Natural convection in an evaporative air-water system inside a cavity heated by an immersed porous medium

Julien Carlier[1, a)] and Miltiadis V. Papalexandris[2, b)]

[1)]*Université catholique de Louvain, Institute of Mechanics, Materials and Civil Engineering, 1348 Louvain-la-Neuve, Belgium*

[2)]*Université catholique de Louvain, Institute of Mechanics, Materials and Civil Engineering, 1348 Louvain-la-Neuve, Belgium*

We report on numerical results of natural convection inside a cavity that is partially filled with water and heated by an immersed porous medium. The part of the cavity above the water is occupied by air. The heat provided by the porous medium generates thermal convection in the water and the air. While water evaporation at the free surface generates convection of vapor in the air too. The porous medium is treated as a continuum and the flow inside and outside of it is modeled via the one-domain approach. Herein we consider two cases at different Rayleigh numbers. In the first case the flow is laminar in the air and transitional in the water, and in the second one the flow in both phases is turbulent. Our simulations predict that thermal convection in each phase is organized in a single or dual-roll large scale circulation. Water descends from the free surface along the edges of the cavity, and near the bottom it moves mostly around the porous medium. Overall the presence of the porous medium increases circulation hence convective heat transport. On the other hand, the free-surface temperature and evaporation rate are essentially constant and subject only to small-amplitude fluctuations. Further, the convective structures of the two fluids interact with one another at the free surface, and the main roll of the water exerts a low-frequency modulation to the those in the gas. These findings can be relevant to industrial applications of water pools.

[a)]Electronic mail: julien.carlier@uclouvain.be

[b)]Corresponding author: miltos@uclouvain.be

I. INTRODUCTION

This paper is concerned with natural convection in an open-top container (pool or cavity) that is partially filled with water. The container is heated by an immersed solid matrix that is assimilated as a porous medium. Above the free surface of the water, the cavity is occupied by humid air. The heat provided by the porous medium generates thermal convection in the water and in the air inside the cavity. Further, the evaporation of water at the free surface generates convective transport of vapor in the air. This configuration is encountered in various industrial applications, such as boilers, thermal power plants, and nuclear power stations. One case of particular interest is thermal convection during the early stages of a loss-of-cooling accident in storage pools of spent nuclear fuel. Under normal operation, decay heat is evacuated via a system of pumps and external heat exchangers. In case of malfunctioning of this system, the water stays in the pool and heat is evacuated via evaporation at the free surface and, eventually, boiling. For modeling purposes, the spent-fuel assemblies can be assimilated as an internally heated porous medium.

Natural convection occurs in numerous natural phenomena and practical applications. The most common case of study is Rayleigh-Bénard convection (RBC), which involves convection of a single fluid between two horizontal boundaries that are maintained at different temperatures. The literature on RBC is vast and the reader is referred to well-known review articles such as[1–4] and the wealth of references provided therein. The problem we consider herein has two distinct features that differentiate it significantly from RBC. The first one is that the working medium is a two-phase system, with the two phases being separated by an evaporative interface. The second one is that the cavity contains a porous medium; in other words, it constitutes a mixed porous-pure fluid domain.

With regard to the first feature, i.e. convection in cavities with an evaporative free surface, most experimental studies were focused on the evaporation rate; see, for instance,[5–10] and the review article[11]. These investigations led to the development of various empirical relations for the evaporation rate in terms of the ambient conditions and the free-surface temperature.

An early numerical study of convection in a cavity was presented by Zikanov et al.[12]. Therein, evaporation was not accounted for and the free surface was modeled as a free-slip plane. The same simplifications were adopted subsequently in the numerical simulations presented in[13,14]. Whereas the numerical studies[15,16] accounted for evaporation by incorporating the evaporation model[10] but also kept fixed the location of the free surface. The authors of a recent study[17] presented numerical simulations of convection in a pool at high turbulence intensities and, on the basis of their findings,

proposed a new scaling law between the Nusselt and Rayleigh numbers. For those simulations, the evaporation model[10] was combined with a remeshing strategy to account for the descent of the free surface.

Nonetheless, in the aforementioned studies, the natural convection above the free surface was not accounted for. In other words, they were simulations with a single-phase working medium. Recent relevant studies[18,19] focused in convection in a box containing two immiscible fluid layers, i.e. without phase change across the free surface. The study[18] was based on the Cahn-Hillard formulation for the volume fraction of one of the two fluids, whereas the simulations of[19] employed the volume-of-fluid approach. Convection in two fluids separated by an evaporative interface was the subject of[20]. The authors of that paper derived a new model for the interface temperature and validated it via 2D numerical simulations. Finally, in[21,22] we presented 3D Direct Numerical Simulations (DNS) of natural convection in an air-water system with evaporation. Therein, the local evaporation rate was computed directly by applying jump relations at the free surface. Also, the descent of the free surface was computed directly via a dynamic tracking algorithm. However, due to excessive computational costs, these simulations were limited to the so-called soft turbulence regime, i.e. at moderate Rayleigh numbers.

In relation to the second feature of the problem (immersed porous medium), thermal convection in mixed porous-pure fluid domains is encountered in a variety of natural phenomena and technological applications as well. Relevant natural phenomena are forest and brush fires, and convection between the earth's porous inner and liquid outer cores[23]. In technological applications, convection in mixed domains is encountered in fuel cells, heat-transfer devices, power stations and elsewhere. In numerical studies of flow in mixed domains, an important aspect is the treatment of the macroscopic interface between the porous and pure-fluid regions.

To this end, two approaches have been developed. The first one is the *two-domain* approach, which employs separate governing equations for each region and matching conditions at the interface[24–27]; see also the monographs[28,29] and the numerous references provided therein. The second one is the *one-domain* approach, which uses the porosity as a field variable over the entire domain and a single set of governing equations that are valid in both porous and pure-fluid regions; see[30–33], as well as the monographs[28,34,35]. Nonetheless, computational studies of turbulent convection in mixed domains are scarce. A notable exception is the recent work of[33] which consisted of 2D simulations. Also, recently, the authors of[36] presented 3D simulations of convection in a cavity driven by an immersed porous medium. Therein, however, the free surface

was treated as a free-slip plane without evaporation.

Most often, computational studies of convection in mixed domains assume thermal equilibrium between the solid matrix and interstitial fluid in the porous region[26,37]. However, this approximation is not always valid, especially when the solid matrix is internally heated. For this reason, various recent studies consider thermal non-equilibrium in the porous region[27,38,39]. This implies that each phase (solid matrix and interstitial fluid) is endowed with its own energy-balance equation[28] and appropriate constitutive relations are introduced to describe the interphasial heat exchange.

In this paper, we extend our earlier studies[21] and present numerical simulations of convection in a cavity that contains water in the lower part and air in the upper one, but is heated by an immersed porous medium. Additionally, we do account for water loss due to evaporation and the corresponding descent of the free surface. With regard to the porous medium, we follow the one-domain approach and consider thermal non-equilibrium between the solid matrix and the interstitial fluid. Accordingly, we solve separate energy equations for the fluid and solid phases. Herein we present numerical results for two cases. In the first one, the thermal convection is transitional in the water and laminar in the gas. This case is treated numerically via DNS. In the second one, the thermal convection belongs to the soft-turbulence regime in both fluids. This case is treated via Large-Eddy-Simulations (LES). The principal objectives of our study are: i) to analyze the convective structures below and above the free surface, ii) to provide physical insight on the interactions between the main convective structures of the two fluids at the free surface, iii) to examine the flow patterns around and inside the porous medium and their impact on convective heat transport.

This paper is structured as follows. In section 2 we describe the mathematical model, including the jump relations at the free surface and the parametrization of interphasial drag and heat exchange in the porous medium. In section 3, we present the setup of the computational domain and outline the mesh-generation strategy. Section 4 consists of the presentation of the numerical results. More specifically, we discuss the main flow patterns in the water and gas columns, provide results for the first and second-order flow statistics, and analyze the power spectra of the thermal fluctuations. Finally, section 5 concludes.

II. MATHEMATICAL MODEL

As mentioned above, the mathematical model is based on the one-domain approach for mixed porous-pure fluid domains. This model is supplemented with appropriate jump conditions at the water-air interface. In this section we present the governing equations and these jump conditions. Also, we outline the parametrization of the coefficients related to interphasial drag and heat exchange.

A. Governing equations

We consider a cuboid with an open-top boundary, i.e. a cavity. It is partially filled with liquid water and the remaining part is occupied by humid air. Additionally, a porous solid matrix is located at the bottom part of the cavity, completely immersed in the water. The solid matrix is assumed to consist of identical, uniformly distributed and parallel cylinders that are perpendicular to the bottom wall. One may assume, for example, that these cylinders are made of steel. The solid matrix emits a heating power Q that induces thermal convection in both the water and the air above. This is accompanied by water evaporation at the free surface and convective transport of vapor in the air. Even though the free-surface temperature, denoted by T_F, evolves with time, the air at the top boundary is assumed to be in contact with atmospheric air at fixed temperature T_c, which is lower than T_F. A schematic illustration of the problem in hand is provided in Fig. 1.

For modeling purposes, the solid matrix is assimilated as a continuous medium with porosity ϕ. The governing system of equations is the low-Mach number approximation of the thermomechanical model[32] for flows in mixed porous and pure-fluid domains, augmented with a transport equation for the water-vapor concentration in air[40],

$$\frac{\partial \phi\rho}{\partial t} + \nabla\cdot(\phi\rho\boldsymbol{u}) = 0, \tag{1}$$

$$\frac{\partial \phi\rho\boldsymbol{u}}{\partial t} + \nabla\cdot(\phi\rho\boldsymbol{u}\boldsymbol{u}) = -\nabla\phi p' + \nabla\cdot(\phi\boldsymbol{\tau}) + \phi g\, y\nabla\rho\ - \boldsymbol{\delta u}, \tag{2}$$

$$c_p\phi\frac{\partial \rho T}{\partial t} + c_p\nabla\cdot(\phi\rho\boldsymbol{u}T) = \phi\frac{\mathrm{d}p_0}{\mathrm{d}t} - \nabla\cdot(\phi\boldsymbol{q}) + \mathcal{H}(T^s - T), \tag{3}$$

$$\frac{\partial \rho Y_\mathrm{v}}{\partial t} + \nabla\cdot(\rho\boldsymbol{u}Y_\mathrm{v}) = -\nabla\cdot\boldsymbol{J}, \tag{4}$$

$$c_p^s(1-\phi)\frac{\partial \rho^s T^s}{\partial t} = (1-\phi)\frac{\mathrm{d}p_0}{\mathrm{d}t} - \nabla\cdot((1-\phi)\boldsymbol{q}^s) - \mathcal{H}(T^s - T) + r\,. \tag{5}$$

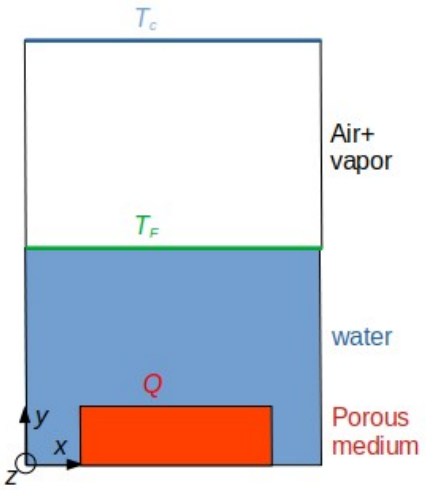


FIG. 1. Schematic illustration of the problem in hand.

Eqs. (1)–(3) are, respectively, the mass, momentum and energy balance laws of the fluid medium and Eq. (4) is the balance law of the mass of water vapor in the gas column. While (5) is the energy balance law for the solid matrix. In other words, we assume thermal non-equilibrium between the two phases in the porous medium. This system is valid everywhere in the cavity, above and below the free surface of water.

In the above system, ρ, $\boldsymbol{u} = (u, v, w)$, and T denote respectively the density, velocity vector and temperature of the fluid. Eq. (4) is the transport equation for the vapor concentration Y_{v}. Further, Eq. (5) is the energy-balance law for the solid matrix, with T^s being its temperature. It is noted that since the solid matrix is at the bottom part of the domain, then $\phi = 1$ everywhere in the air column; as such, ϕ does not enter (4).

In the energy equation (3) p_0 stands for the thermodynamic pressure, i.e. the first-order terms in the low-Mach number expansion of the pressure field. Since the flow domain is open, the p_0 is constant and equal to the atmospheric pressure, 1 bar. Moreover, p' stands for the piezometric pressure[38] and reads,

$$p' = p + \rho g y, \tag{6}$$

with p being the sum of the dynamic and bulk viscous pressures[41]. Also, g is the gravitational acceleration and y is the spatial coordinate in the vertical direction (opposite to gravity).

Further, in the system (1)-(5), $\boldsymbol{\tau}$, $\boldsymbol{q}$, $\boldsymbol{q}^s$, $\boldsymbol{J}$ denoted respectively the viscous-stress tensor, heat-flux

vectors and vapor mass-flux vector,

$$\boldsymbol{\tau} = 2\mu(\boldsymbol{S} - \frac{1}{3}(\nabla \cdot \boldsymbol{u})\boldsymbol{I}), \tag{7}$$

$$\boldsymbol{q} = -\lambda \nabla T, \tag{8}$$

$$\boldsymbol{q}^s = -\boldsymbol{\lambda}^s \nabla T^s, \tag{9}$$

$$\boldsymbol{J} = -\rho \mathcal{D} \nabla Y_{\mathrm{v}}, \tag{10}$$

with $\boldsymbol{I}$ being the identity matrix and $\boldsymbol{S} = \frac{1}{2}(\nabla \boldsymbol{u} + (\nabla \boldsymbol{u})^\top)$ the strain-rate tensor. Further, μ is the dynamic viscosity of the fluid, λ its thermal conductivity, and $\mathcal{D}$ is the molecular diffusivity of water vapor in air. Further, $\boldsymbol{\lambda}^s$ is the thermal conductivity of the solid matrix. In general, the matrix is anisotropic and, therefore, $\boldsymbol{\lambda}^s$ is a second-order tensor. Finally, $\boldsymbol{\delta}$ is the tensor of interphasial-drag coefficients, $\mathcal{H}$ is the coefficient of interphasial heat transfer; their parametrization is elaborated in section II B below.

With regard to the energy equations (3) and (5), since p_0 is constant, then the sensible enthalpy h_{sens} of all phases is a function of the temperature only; in particular, $dh_{\mathrm{sens}} = c_p dT$, where c_p refers to the specific heat capacity under constant pressure. While r is the volumetric heat-source term due to the internal heating of the solid matrix.

In terms of notation, the superscripts l, g and s will henceforth refer to variables related to the water, air-vapor mixture, and solid matrix, respectively. Also since Eqs. (1)-(3) are valid for both phases, thermophysical properties such as density and temperature are written in a unified manner via the indicator function I, i.e.

$$\rho = \rho^l + I(\rho^g - \rho^l), \tag{11}$$

with $I = 1$ in the gas column and $I = 0$ in the water column.

The air-vapor mixture is assumed to obey the ideal-gas law,

$$p_0 = \rho^g \frac{R_u}{M^g} T^g, \tag{12}$$

with R_u being the universal gas constant and M^g the molar mass of the gaseous mixture. The latter one is calculated in terms of molar masses of dry air and water, M_a and M_v, respectively,

$$M^g = \left(\frac{1 - Y_v}{M_a} + \frac{Y_v}{M_v} \right)^{-1}, \tag{13}$$

A Sutherland-type law is used to model the variation of the dynamic viscosity μ^g and thermal conductivity λ^g of the gas with the temperature,

$$\mu^g = \mu_c^g \left(\frac{T^g}{T_c} \right)^{0.7}, \qquad \text{and} \qquad \lambda^g = \lambda_c^g \left(\frac{T^g}{T_c} \right)^{0.7}, \tag{14}$$

where μ_c^g and λ_c^g stand for the dynamic viscosity and thermal conductivity of ambient air at T_c. Also, c_p^g, is the specific heat capacity of the gas and is assumed to be equal to that of ambient air. The molecular diffusivity in the air-vapor mixture is obtained by using the following relation[42],

$$\mathcal{D} \;=\; 1.87\times10^{-10}\;\frac{T^{g^{2.072}}}{p_0}\,, \tag{15}$$

with $p_0 = 1$ bar.

With regard to the liquid water, we employ an isobaric equation of state. Accordingly, its density is considered to depend only on the temperature. More specifically, we employ a fourth-order polynomial fit of the tabulated data of[43],

$$\rho^l \;=\; c_4 T^{l^4} + c_3 T^{l^3} + c_2 T^{l^2} + c_1 T^l + c_0\,, \tag{16}$$

where c_0 - c_4 are the polynomial coefficients. Additionally, fourth-order polynomial fits of the data of[43] are used to approximate the values of the heat capacity, dynamic viscosity and thermal conductivity of the liquid water. The values of the coefficients in these fits for the temperature range of interest can be found in[16].

The thermophysical properties of the solid matrix are those of steel and their values can be found in[36]. With regard to the thermal-conductivity tensor $\boldsymbol{\lambda}^s$, the solid matrix consists of parallel vertical cylinders, which means that it is orthotropic. Therefore, only its diagonal elements are non-zero. Moreover, the cylindrical elements are assumed to be of small diameter and are not connected. Therefore, $\lambda^s_{11} = \lambda^s_{33} = 0$, whereas $\lambda^s_{22} = \lambda^s$ with λ^s the thermal conductivity of steel.

B. Parametrization of the coefficients related to interphasial drag and heat exchange

Below we outline the parametrization of the coefficients related to interphasial drag and heat exchange, $\boldsymbol{\delta}$ and $\mathcal{H}$ respectively, that enter Eqs. (2), (3) and (5). A more detailed description of this procedure is provided in[36].

As mentioned above, the solid matrix is an orthotropic medium. Therefore, only the diagonal elements of $\boldsymbol{\delta}$ (i.e. δ_{11}, δ_{22} and δ_{33}) are non-zero and, furthermore, $\delta_{11} = \delta_{33}$. For the parametrization of δ_{11} we start with the expression provided in[44] for the average horizontal drag on a single cylinder of height h_p and diameter d_c. This expression reads,

$$f \;=\; h_p \mu^l u (k_0 + k_2 Re^2_{d_c})\,, \tag{17}$$

where Re_{d_c} is the Reynolds number based on the local horizontal fluid velocity and cylinder diameter, $Re_{d_c} = \frac{d_c\sqrt{u^2+w^2}}{\nu^l}$, where $\nu^l = \frac{\mu^l}{\rho^l}$ is the water's kinematic viscosity. Further, k_0 and k_2 are empirical coefficients the values of which are provided in[44]. Then, δ_{11} is computed as the product between f/u and the number density of cylinders $N_c = 4(1-\phi)/\pi d_c^2 h_p$. The resulting expression is,

$$\delta_{11} \;=\; \delta_{33} \;=\; \frac{4\mu^l(1-\phi)}{\pi d_c^2}(k_0 + k_2 Re_{dc}^2)\,. \tag{18}$$

For the parametrization of δ_{22}, following[32], we first consider the wall stress $\tau_w = \frac{1}{2}c_f\rho^l v^2$ exerted by a 2D flow over a flat plane. For the skin friction coefficient c_f we employ the average value over the cylinder height[45], $c_f = 1.328\sqrt{\nu^l/(|v|h_p)}$. Then δ_{22} is approximated as the product between τ_w/v, the surface area of a single cylinder $\pi h_p d_c$ and the number density of the cylinders N_c. The final relation is,

$$\delta_{22} \;=\; 2.656\frac{(1-\phi)}{d_c}\sqrt{\frac{\mu^l\rho^l|v|}{h_p}}\,. \tag{19}$$

On the other hand, the interphasial heat exchange, $\mathcal{H}$, is a scalar. In absence of conclusive experimental data, we assume that it can be parameterized as the sum of two contributions[36]. The first one, $\mathcal{H}_\perp$, is due to the cross flow of the fluid, while the second one, $\mathcal{H}_{||}$, is due to the flow parallel to the cylindrical elements. To estimate $\mathcal{H}_\perp$, we multiply the heat-transfer coefficient for flow around a cylinder[45] with the number density N_c. Similarly, to estimate $\mathcal{H}_{||}$, we consider the heat-transfer coefficient for flow parallel to a flat plate and multiply it by the perimeter of a cylindrical element and the number density N_c. The resulting expressions read,

$$\mathcal{H}_\perp \;=\; \frac{4(1-\phi)}{d_c^2}\lambda^l Nu_{d_c}\,, \qquad \mathcal{H}_{||} \;=\; \frac{4(1-\phi)}{d_c h_p}\lambda^l Nu_{h_p}\,, \tag{20}$$

with Nu_{d_c} and Nu_{h_p} being the Nusselt numbers based on the cylinder diameter and height, respectively. They are computed from the following empirical correlations[45],

$$Nu_{d_c} \;=\; CRe_{d_c}^m Pr^{1/3}\,, \qquad Nu_{h_p} \;=\; 0.453Re_{h_p}^{0.5}Pr^{1/3}\,, \tag{21}$$

where C and m are functions of Re_{d_c} and Re_{h_p}, the latter one being the Reynolds number based on the cylinder height, $Re_{h_p} = \frac{vh_p}{\nu^l}$. Finally, $\mathcal{H}$ is computed by adding $\mathcal{H}_\perp$ and $\mathcal{H}_{||}$,

$$\mathcal{H} \;=\; \mathcal{H}_\perp + \mathcal{H}_{||} \;=\; \frac{4(1-\phi)}{d_c}\lambda^l\left(\frac{Nu_{d_c}}{d_c} + \frac{Nu_{h_p}}{h_p}\right). \tag{22}$$

C. Jump relations across the air-water interface

The governing system of balance laws (1)–(4) is closed with jump conditions of the flow variables at the air-water interface, i.e. at the free surface of the water. The jump of a generic variable q from the water side to the gas side is denoted by $[q] = q^l - q^g$. In our study, the free surface, denoted by F, is approximated as a flat horizontal plane. For the physical and geometrical parameters considered herein, this assumption has been validated on the basis of the work of Liu et al.[46] on two-layer thermally driven turbulence. Additionally, Marangoni effects are not included in the governing system of equations. The validity of these two assumptions is discussed in subsection IV.C in which we discuss flow statistics. Below we list the jump relations across F. Details on their derivation can be found in[47]; see also[40,48,49].

- Temperature,
$$[T] \;=\; 0\,, \qquad \left[\lambda \frac{\partial T}{\partial y}\right] \;=\; -\dot{m}''\, L^{lg}\,, \tag{23}$$
with $\dot{m}''$ the local evaporative mass flux and L^{lg} the latent heat of evaporation of water.

- Density,
$$[\rho] \;=\; \rho^l(T_F, p_0) - \rho^g(T_F, p_0)\,, \tag{24}$$
with T_F the local temperature at the free surface.

- Vapor mass fraction,
$$[Y_{\rm v}] \;=\; 1 - Y_{v,F}\,, \qquad \text{and} \quad -\rho^g\, \mathcal{D}\, \frac{\partial Y_v}{\partial y} \;=\; \dot{m}''(1 - Y_{v,F}) \quad \text{at } F\,, \tag{25}$$
with $Y_{v,F}$ the mass fraction of water vapor at the free surface.

- Normal velocity component,
$$[v] \;=\; \dot{m''}\,(\frac{1}{\rho^l} - \frac{1}{\rho^g})\,, \qquad \text{and} \quad v^l \;=\; 0\,, \quad v^g \;=\; -\dot{m''}\left(\frac{1}{\rho^l} - \frac{1}{\rho^g}\right) \quad \text{at } F\,. \tag{26}$$

- Tangential velocity components,
$$[u] \;=\; [w] \;=\; 0\,, \qquad \left[\mu \frac{\partial u}{\partial y}\right] \;=\; \left[\mu \frac{\partial w}{\partial y}\right] \;=\; 0\,. \tag{27}$$

- Piezometric pressure,
$$[p'] \;=\; \dot{m''}^2 \left(\frac{1}{\rho^g} - \frac{1}{\rho^l}\right) + [\rho]\, g\, h + \left[2\mu \frac{\partial v}{\partial y} - \frac{2}{3}\mu \nabla \cdot \boldsymbol{u}\right], \tag{28}$$
where h is the distance between the free surface and the bottom wall, *i.e.* the instantaneous height of the water column.

D. Subgrid scale modeling and numerical method

In this paper we present results for two cases, corresponding to different Rayleigh numbers intensities. For case 1 (low Rayleigh-number case) we have performed DNS, and for case 2 (higher Rayleigh numbers) we have performed wall-resolved LES for the purposes of computational savings. Accordingly, in case 2, u, T and Y_v are Favre-averaged quantities. Also, in the case of LES, the subgrid stress tensor $\boldsymbol{\tau}^t$, the subgrid heat flux $\boldsymbol{q}^t$ and the subgrid mass flux $\boldsymbol{J}^t$ are added on the right-hand side of Eqs. (2), (3) and (4), respectively.

The subgrid modeling is the same in[50] and is based on the eddy-viscosity approach, according to which $\boldsymbol{\tau}^t$ represents additional viscous stresses. As such, its deviatoric component reads,

$$\boldsymbol{\tau}^t - \frac{1}{3}\mathrm{tr}(\boldsymbol{\tau}^t)\boldsymbol{I} \;=\; -2\mu_t\left(\boldsymbol{S} - \frac{1}{3}\left(\nabla\cdot\boldsymbol{u}\right)\boldsymbol{I}\right), \tag{29}$$

where μ_t is the turbulent (eddy) viscosity. In the present study, μ_t is computed via the WALE model[51]. The subgrid scalar fluxes are modeled via the standard gradient assumption as follows,

$$\boldsymbol{q}^t \;=\; -\lambda_t\nabla T, \tag{30}$$

$$\boldsymbol{J}^t \;=\; -\rho\mathcal{D}_t\nabla Y_\mathrm{v}, \tag{31}$$

in which λ_t and $\mathcal{D}_t$ stand for the turbulent thermal conductivity and diffusivity, respectively. λ_t is computed via the Reynolds analogy $\lambda_t = \frac{\mu_t c_p}{Pr_t}$. The turbulent Prandtl number Pr_t is set equal to 0.4, as suggested in[52] for thermal-convection problems. Further, in the present study we assume that the turbulent Lewis number is equal to unity, $Le_t = \frac{\lambda_t}{\rho c_p \mathcal{D}_t} = 1$. Consequently, the turbulent molecular diffusivity reads $\mathcal{D}_t = \frac{\mu_t}{\rho Pr_t}$. With regard to Le_t, the selected value (unity) is common in flame simulations but there is no specific guidance in the literature on its value for combined thermal and species convection. For this reason, we performed LES of the flow studied in[21] with $Le_t = 1$. The LES predictions compared well with the DNS results[21]. Accordingly, we used $Le_t = 1$ in the present study as well.

The governing system (1)–(5), together with the associated jump conditions (23)–(28), is discretized and solved numerically via a numerical method that combines a low-Mach number solver with an interface-tracking algorithm. The low-Mach number solver is the generalization of the finite-volume, time-accurate algorithm[53] to flows in mixed porous-pure fluid domains, following the one-domain approach[31,32]. It involves a predictor-corrector time-marching scheme and a projection method for the computation of the piezometric pressure and velocity fields. It is

2nd-order accurate in space and time. Spatial derivatives are computed via centered differences. The various term are integrated explicitly in time via an Adams-Bashforth scheme, except for the diffusive fluxes in the vertical direction for which a semi-implicit Crank-Nicolson scheme is employed. The algorithm has been implemented in a collocated grid arrangement and incorporates a flux-interpolation technique to remedy the odd-even decoupling problem associated with such grids. It has been validated via a series of numerical test cases[54] and has been employed in simulations of related thermal convection problems[36,38].

The tracking of the free surface is performed via the algorithm[40] which is based on the ghost-fluid method. This tracking algorithm has been validated via a series of test cases[40], including comparisons against experimental data of convection in water-air systems with evaporation. Since then, we have employed it in various studies of thermal convection in air-water systems[21,22].

The entire numerical method has been implemented in a C/C++ code and parallelized via the MPI protocol. It uses the PETSc library of data structures and parallel linear solvers[55]. The Poisson equation for the pressure is solved with the PFMG routine of PETSc which is based on a parallel semi-coarsening multigrid solver.

III. NUMERICAL SETUP

In this section we present the configuration of the computational domain and outline the mesh-generation strategy.

A. Configuration of the computational domain

As mentioned above, the computational domain is a cavity in the form of a cuboid. It is partially filled with liquid water and contains a porous medium placed on the bottom wall. Thus we may assume that the flow domain consists of three regions or sub-domains. In order to fix ideas, let H and W denote the height and horizontal dimensions of the cavity. Also, let h_p denote the height of the porous medium, and h the instantaneous height of the water. Initially, $h = h_0$. The three regions are the following.

i. $0 < y \leq h_p$. This is the bottom region of the flow domain. It encompasses the porous medium and terminates at the macroscopic horizontal interface between the solid matrix and water. For brevity of expression, this region will henceforth be referred to as the *porous-medium*

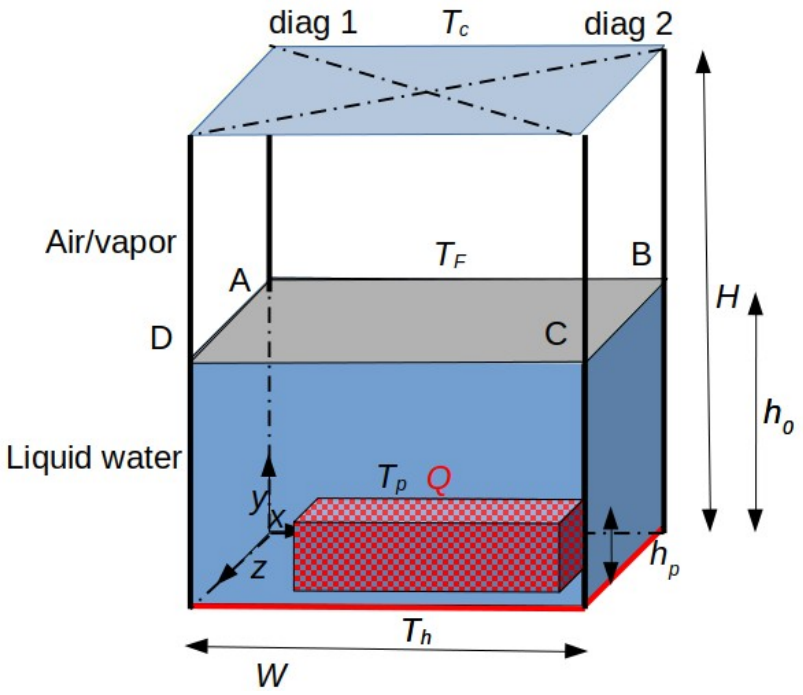


FIG. 2. Configuration of computational domain. The diagonal planes are denoted by 1 and 2, and the letters A, B, C and D refer to the four vertical edges of the cavity. The porous medium (shown in red) is immersed in the water and emits a heating power Q.

region.

ii. $h_p < y \leq h$. This is the region above the porous structure and up to the free surface. It will henceforth be referred to as the *pure-water region*.

iii. $h < y < H$. This is the region above the water's free surface that it occupied by humid air. It is referred to as the *gas column*.

Since the first two regions are filled with water, they are collectively referred to as the *water column*. The porous medium is centrally placed above the bottom wall and is assumed to occupy a volume V_p. Let a_p being the ratio between the area of its bottom surface and the area of the bottom wall; this quantity is referred to as the *area coverage* of the porous medium. Then, $V_p = h_p a_p W^2$. The configuration of the computational domain is presented schematically in Fig. 2.

Next, for purposes of non-dimensionalization, we introduce reference values of the various flow variables. The reference length is the initial height of the pure-water region, $l_{ref} = h_0 - h_p$. The reference pressure is p_0. Since the convective patterns in the water and gas columns are different, it is convenient to employ separate reference temperatures for the water and gas columns. For

this purpose, we recall that T_c, T_h, and T_F denote, respectively, the temperature at the open top boundary, bottom wall, and free surface. We also introduce T_p, the water temperature at the top of the solid matrix, i.e. at $y = h_p$. As mentioned above T_c is constant and uniform, while the other temperatures vary along the corresponding horizontal planes and in time.

The reference temperature in the water column, T^l_{ref}, is defined to be the average between the initial values of T_p and T_F. Similarly, the reference temperature in the gas column, T^g_{ref}, is the average between T_c and the initial value of T_F. Thus, the reference thermodynamic state of the water is determined by (p_0, T^l_{ref}) and that of the gas by (p_0, T^g_{ref}). The top-bottom temperature difference in the pure-water region and in the gas column are denoted by $\Delta T^l = T_p - T_F$ and $\Delta T^g = T_F - T_c$, respectively. The reference velocity is the free-fall velocity in the pure-water region, $u_{\text{ff}} = \sqrt{g l_{ref} \beta^l \Delta T^l}$ where β^l is the thermal expansion coefficient of water at its reference state. Also, the free-fall time, $t_{\text{ff}} = \frac{l_{ref}}{u_{\text{ff}}}$, is the reference time-scale.

The solid matrix emits a heating power Q, given by $Q = \int_{V_p} (1-\phi) r \, dV$. The volumetric heating rate r is constant and uniform. The emitted heat establishes temperature gradients in the normal direction and convective motions in both columns.

With regard to dimensionless numbers, we introduce one set for the pure-water region and one for the gas column. For the pure-water region, the Prandtl, Rayleigh, and Reynolds numbers are given by

$$Pr^l = \frac{\nu^l}{\alpha^l}, \qquad Ra^l = \frac{g\beta^l \Delta T^l \, l^3_{ref}}{\nu^l \alpha^l}, \quad Re = \frac{u_{\text{ff}} \, l_{ref}}{\nu^l}, \tag{32}$$

with $\alpha^l = \frac{\lambda^l}{\rho^l \, c^l_p}$ the thermal diffusivity and ν^l the kinematic viscosity of water at the reference state. For the gas column, the Prandtl, Rayleigh, Reynolds and Lewis numbers are given by

$$Pr^g = \frac{\nu^g}{\alpha^g}, \qquad Ra^g = \frac{g\beta^g \Delta T^g (H-h_0)^3}{\nu^g \alpha^g}, \quad Re = \frac{\sqrt{g\beta^g \Delta T^g}(H-h_0)^{\frac{3}{2}}}{\nu^g}, \qquad Le^g = \frac{\alpha^g}{\mathcal{D}}, \tag{33}$$

with the thermal diffusivity $\alpha^g = \frac{\lambda^g}{\rho^g \, c^g_p}$ and the kinematic viscosity ν^g taken at the reference state of dry air. Two more significant dimensionless groups are the initial aspect ratios of the water and gas columns, Γ^l and Γ^g, respectively. These are given by $\Gamma^l = \frac{W}{l_{ref}}$ and $\Gamma^g = \frac{W}{(H-h_0)}$.

In the present study, we consider two cases. In case 1, the Rayleigh number in the pure-water region is estimated at $Ra^l = 3.45 \times 10^5$, which corresponds to thermal convection in the transitional regime. While the Rayleigh number in the gas column is $Ra^g = 10^4$ which corresponds to laminar thermal convection. This case is treated numerically via DNS. In case 2, the turbulence intensities are higher; the estimated Rayleigh numbers in the pure-water region and gas column

TABLE I. Estimated dimensionless numbers in the pure-water region and the gas column.

	Ra^l	Re^l	Pr^l	Ra^g	Re^g	Pr^g	Le^g
case 1	3.45×10^5	271	4.72	10^4	120	0.73	0.82
case 2	1.3×10^6	554	4.21	10^6	1217	0.73	0.82

TABLE II. Geometrical parameters of the computational domain.

	W (m)	H (m)	h_0 (m)	l_{ref}	h_p	ϕ	a_p
case 1	0.0225	0.050625	0.028125	0.0225	0.005625	0.6	0.64
case 2	0.0325	0.130625	0.040625	0.0325	0.008125	0.6	0.64

are $Ra^l = 1.3\times10^6$ and $Ra^g = 10^6$, respectively. Accordingly, thermal convection in both columns belongs to the soft-turbulence regime. As mentioned above, for purposes of computational savings, this case is treated numerically via LES. The dimensionless numbers for both cases are provided in Table I.

With regard to geometrical parameters, we note that the height H and width W of the cavity are higher in case 2 than in case 1. Further, the aspect ratio of the gas column in case 1 is $\Gamma^g = 1$, while in case 2 it is $\Gamma^g = 0.36$. On the other hand, the aspect ratio of the pure-water region is kept the same, $\Gamma^l = 1$ in both cases. The porosity of the porous medium is $\phi = 0.6$. Its width is $0.8\,W$ and therefore its area coverage $a_p = 0.64$. Its height is one fifth of the initial height of the free surface, $h_p = \frac{h_0}{5}$. The diameter of the cylindrical elements of the solid matrix is taken to be $d_c = 0.001 l_{ref}$, which implies that they are thicker in case 2. The values of the various geometrical parameters in the two cases are given in Table II.

In terms of boundary conditions, the bottom and vertical boundaries are assumed to be rigid and adiabatically isolated walls. Therefore the no-slip kinematic condition and the zero-Neumann thermal condition are prescribed at them. A zero-Neumann condition is also assigned to the vapor concentration at the vertical walls. The top boundary is assumed to be open. Therefore the temperature and vapor concentration therein are constant and equal to the ambient ones. These are $T_c = 298.15$ K, and $Y_v^{\text{amb}} = 0.0074$ which corresponds to an ambient relative humidity of 40%.

With regard to the kinematic boundary condition at the top, we note that mass conservation

TABLE III. Thermal parameters for cases 1 and 2. The values of T_h and T_F are the initial ones.

	T_c (K)	T_h (K)	T_F (K)	T^l_{ref} (K)	ΔT^l (K)	ΔT^g (K)	Q (mW)	r (mW/cm^3)
case 1	298.15	309	307.8	308.3	1	9.65	71.25	97.74
case 2	298.15	315	313.5	314.0	1	15.35	213.75	97.29

requires that the evaporative flux at the free surface and at the top be equal. This implies that water vapor is exiting from the top. Accordingly, the following Dirichlet condition is assigned to the vertical velocity component therein, v^g_{top},

$$v^g_{top} \;=\; \frac{1}{\rho^g_{top} W^2} \int_F v^g \rho^g \, dx dz \,. \tag{34}$$

For the horizontal velocity components at the top, we prescribe a convective boundary condition[56] with the convective velocity being equal to v^g_{top}. For more details on the implementation of the kinematic conditions at the open top boundary, the reader is referred to[21].

We further recall that the energy balance law for the solid matrix (5) is valid only in the porous region. This necessitates the prescription of a thermal condition at the macroscopic porous-pure fluid interface. Herein we prescribe the following condition

$$(1-\phi)\boldsymbol{\lambda}^s \nabla T^s \cdot \boldsymbol{n} \;=\; 0\,, \tag{35}$$

where $\boldsymbol{n}$ is the unit vector normal to the macroscopic interface. This boundary condition is discussed in more detailed in[32,38].

Finally, with regard to initial conditions, both fluids are assumed to be at rest. We also prescribe linear profiles for the initial temperature: from T_h to T_F in the water, and from T_F to T_c in the gas. The initial values of T_h and T_F are calculated via a preliminary simulation on a coarse mesh for the given heating power of the solid matrix. These preliminary simulations also furnish the estimates for the Rayleigh numbers that are listed in Table I. The thermal parameters for our simulations, including heating power Q and volumetric heat source term r, are listed in Table III.

B. Mesh generation

The simulations are performed in a structured mesh consisting of cubical elements. For the simulation of case 1, the mesh generation follows the same procedure as in[13,15]. It is based on the

grid-resolution criteria of[57–59] for DNS of Rayleigh-Bénard convection. These criteria involve the Nusselt numbers which, in our study, is not known a priori. Accordingly, we apply them by using estimates that are computed from the preliminary simulations mentioned above.

The first criterion relates to the resolution of the near-boundary regions and the second one to the resolution in the bulk of the domain. According to[57] and for $Pr > 3$ (which is the case of liquid water), the dimensionless thicknesses of the thermal and hydrodynamic boundary layers, δ_θ and δ_u respectively, can be estimated by,

$$\frac{\delta_\theta}{l_{ref}} = \frac{1}{2Nu^l}, \qquad \text{and} \qquad \frac{\delta_u}{l_{ref}} = \frac{1}{2ENu^l}(Pr^l)^{\frac{1}{3}}, \tag{36}$$

where Nu^l is the Nusselt number in the water column and $E = 0.982$. The minimum numbers of cells needed to resolve the hydrodynamic and thermal boundary layers, N_θ and N_u respectively, are given by,

$$N_\theta = \sqrt{2}aE^{\frac{3}{2}}(Nu^l)^{\frac{1}{2}}, \qquad N_u = \sqrt{2}aE^{\frac{1}{2}}(Nu^l)^{\frac{1}{2}}(Pr^l)^{\frac{1}{3}}, \tag{37}$$

with $a = 0.482$.

For $Pr < 3$ (which is the case of air), the thicknesses of the boundary layers are approximated as follows,

$$\frac{\delta_\theta}{l_{ref}} = \frac{1}{2Nu^g}, \qquad \frac{\delta_u}{l_{ref}} = \frac{1}{2Nu^g}(Pr^g)^{0.357-0.022\ ln(Pr^g)}. \tag{38}$$

In this case, the minimum numbers of cells required to resolve the boundary layers are given by,

$$N_\theta = \sqrt{2}a(Nu^g)^{\frac{1}{2}}(Pr^g)^{-0.0355+0.033\ln(Pr^g)}, \qquad N_u = \sqrt{2}a(Nu^g)^{\frac{1}{2}}(Pr^g)^{0.3215+0.011\ln(Pr^g)}. \tag{39}$$

In a DNS, the mesh in the bulk should be sufficiently fine so as to resolve all essential turbulent scales. Herein we employ the criterion of[58] for the bound on the maximum size of a computational cell Δ; see also[59]. This criterion is based on estimates for the smallest hydrodynamic (Kolmogorov) and thermal (Corrsin) scales, η_K and η_C respectively. In the water column, $Pr > 1$ and the smallest turbulent scale is the thermal one. Whereas in the gas column, $Pr < 1$ and the smallest scale is the hydrodynamic one. Therefore, the criterion of[58] in the pure-water region and gas column reads,

$$\frac{\Delta}{l_{ref}} \leq \pi\eta_C = \pi\left(\frac{1}{Ra^l\ Pr^l\ Nu^l}\right)^{\frac{1}{4}}, \qquad \frac{\Delta}{l_{ref}} \leq \pi\eta_K = \pi\left(\frac{(Pr^g)^2}{Ra^g\ Nu^g}\right)^{\frac{1}{4}}. \tag{40}$$

In our study, case 2 is treated numerically via wall-resolved LES. Accordingly, for the grid resolution in the near-boundary regions we apply the same criteria as for the DNS (mentioned

TABLE IV. Mesh properties in the water column. $N_{x,z}$ is the number of cells in each horizontal direction, and N_y in the y direction. Δ is the maximum allowable cell size according to (40) for case 1 and (43) for case 2. $\Delta_{y,max}$ is the maximum height of the computational cells. N_u and N_θ are the numbers of cells in the hydrodynamic and thermal boundary layers. The numbers in parentheses are as follows. 3rd column: total number of cells in the y direction. 7th and 8th columns: minimum number of cells required for the resolution of the boundary layers.

	$N_{x,z}$	N_y	Nu^l (estim.)	δ_u/l_{ref}	δ_θ/l_{ref}	N_u	N_θ	Δ/l_{ref}	$\Delta_{y,max}/l_{ref}$
Case 1	40	53 (94)	13	0.066	0.0384	5 (5)	3 (3)	0.0463	0.038
Case 2	20	28 (90)	18	0.046	0.028	5 (5)	3 (3)	0.135	0.132

above). For the resolution in the bulk, we apply the same criterion in the bulk as in[13,17]. This is based on the following estimate of the Taylor microscale[60],

$$\frac{\eta_{Tay}}{l_{ref}} = \frac{\sqrt{15}u^*}{\sqrt{Ra(Nu-1)}}. \tag{41}$$

with u^* being a representative fluid velocity in the bulk,

$$u^* = \sqrt{0.068Ra^{0.91} + 0.012Ra^{0.96}}. \tag{42}$$

The maximum allowable cell size in the bulk is then given by

$$\frac{\Delta}{l_{ref}} \leq \min(4\eta_C, 4\eta_K, \frac{\eta_{Tay}}{2}). \tag{43}$$

Once the sizes of the near-wall and center cells are fixed, the cell sizes are stretched from the walls to the center via a hyperbolic tangent function and in such a way that the boundary layers are fully resolved. The mesh properties in the water and gas columns are listed in Tables IV and V, respectively.

For the computation of the time increment, Δt, we employ the CFL condition for the convective terms of the governing equations and the condition from the von Neumann stability analysis for the diffusive terms. These conditions are,

$$C_C = \max\left(\frac{u}{\Delta x}, \frac{v}{\Delta y}, \frac{w}{\Delta z}\right)\Delta t \leq 1, \tag{44}$$

and

$$C_D = \max\left(\frac{\nu}{\min(\Delta x, \Delta y, \Delta z)^2}, \frac{\alpha}{\min(\Delta x, \Delta y, \Delta z)^2}, \frac{\mathcal{D}}{\min(\Delta x, \Delta y, \Delta z)^2}\right)\Delta t \leq \frac{1}{2}, \tag{45}$$

TABLE V. Mesh sizes, estimated Nusselt number Nu^g and grid-resolution requirements for the gas column. Δ is the maximum allowable cell size according to (40) and (43). All other symbols are the same as in table IV.

	$N_{x,z}$	N_y	Nu^g (estim.)	δ_u/l_{ref}	δ_θ/l_{ref}	N_u	N_θ	Δ/l_{ref}	$\Delta_{y,max}/l_{ref}$
Case 1	40	41 (94)	2.85	0.156	0.175	9 (2)	10 (2)	0.206	0.0344
Case 2	20	62 (90)	12	0.039	0.044	8 (3)	8 (3)	0.1848	0.121

respectively. In our simulations, we set $C_C = C_D = 0.08$ for case 1 and $C_C = C_D = 0.04$ for case 2. The time increment is then set equal to the smallest value computed from these two conditions.

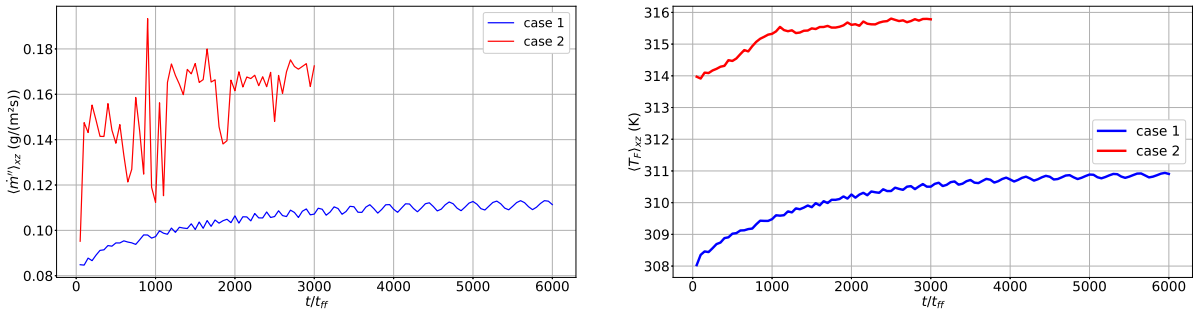
Finally, it is worth adding that the simulations have been performed in a parallel server with Intel® Xeon® Gold-6248 CPUs. For case 1, using 80 cores, the simulation of the flow for 1 $t_{\rm ff}$ takes approximately 15 minutes. For case 2, using 20 cores, the simulation for 1 $t_{\rm ff}$ takes approximately 33 minutes.

IV. NUMERICAL RESULTS

In this section, we present and discuss the results of our simulations for cases 1 and 2 described above. In our presentation, velocities are scaled with the free-fall velocity in the pure-water region $u_{\rm ff}$ and the free-fall time $t_{\rm ff}$ is used for the scaling of time periods and frequencies. Further, we make use of normalized y coordinates, $\frac{y}{l_{ref}}$ in the water column and $\hat{y} = \frac{y-h_0}{H-h_0}$ in the gas column. In terms of notation, the time average of a generic quantity q is denoted by $\langle q \rangle_t$, the xz area average by $\langle q \rangle_{xz}$, and the combined time and area average by $\langle q \rangle$. The latter one will be referred to simply as the mean q.

A. Evolution toward statistically stationary flow

In our study we launch the simulations with the initial conditions mentioned above. Flow statistics are taken once the flow becomes statistically stationary. It is noted that, strictly speaking, the flow never reaches stationary state because the free surface descends continuously due to evaporation. For this reason, the tracking algorithm that computes the location of the free surface is not activated during the long transient stage but only once the flow becomes statistically stationary.



(a) evaporative flux. **(b) free-surface temperature.**

FIG. 3. Evolution of the area-averaged evaporative mass flux $\langle \dot{m}'' \rangle_{xz}$ (a) and the area-averaged free-surface temperature $\langle T_F \rangle_{xz}$ (b).

In other words, during the transient stage, the height of the free surface is kept fixed.

The evolution of the area-averaged evaporative flux $\langle \dot{m}'' \rangle_{xz}$ in the transient stage of both cases is plotted in Fig. 3a. (The term "area-averaged evaporative flux" refers to the evaporative flux averaged over the free surface). While the evolution of the area-averaged free-surface temperature is plotted in Fig. 3b. In case 1, both $\langle \dot{m}'' \rangle_{xz}$ and $\langle T_F \rangle_{xz}$ increase slowly and smoothly with time. Furthermore, they are both subject to small-amplitude, low-frequency oscillations. The frequency is higher at early times but becomes progressively lower. Nonetheless, the oscillation amplitude increases mildly with time.

The observed oscillations are characteristic of thermal convection in the transitional regime[61]. In particular, they persist and do not decay with time. Nonetheless, the values of $\langle \dot{m}'' \rangle_{xz}$ and $\langle T_F \rangle_{xz}$ remain at the same levels after 6000 t_{ff}, which implies that, at that time instance, the flow has become fully developed (statistically stationary).

On the other hand, in case 2, the evolution of $\langle \dot{m}'' \rangle_{xz}$ and $\langle T_F \rangle_{xz}$ is markedly different. They both increase slowly over time but exhibit random fluctuations. The amplitude of the fluctuations of the free-surface temperature is much smaller than in case 1. However, the oscillations of the evaporative flux can be quite high, especially in the early stages. The profiles of both variables stabilize at 3000 t_{ff}, at which time we assume that statistical stationarity has been reached.

It is important to add that since the relevant time periods are quite long, the plots shown in Fig. 3 are produced using a low sampling rate of data, namely, one data point per 50 t_{ff}. For this reason, the actual oscillation frequency of $\langle \dot{m}'' \rangle_{xz}$ and $\langle T_F \rangle_{xz}$ in case 1 is higher than the one inferred from the plots of Fig. 3. Nonetheless, the trends depicted in these plots are accurate.

B. Convective structures in fully developed flow

In this section, we present results for the flow properties and structures in the statistically stationary regime (fully developed flow). For this part of the simulation, the tracking algorithm for the free-surface descent is activated and time statistics are taken over a period of 500 t_{ff}. Such period is deemed sufficient to compute reliable flow statistics for thermal convection in air-water systems[21,22].

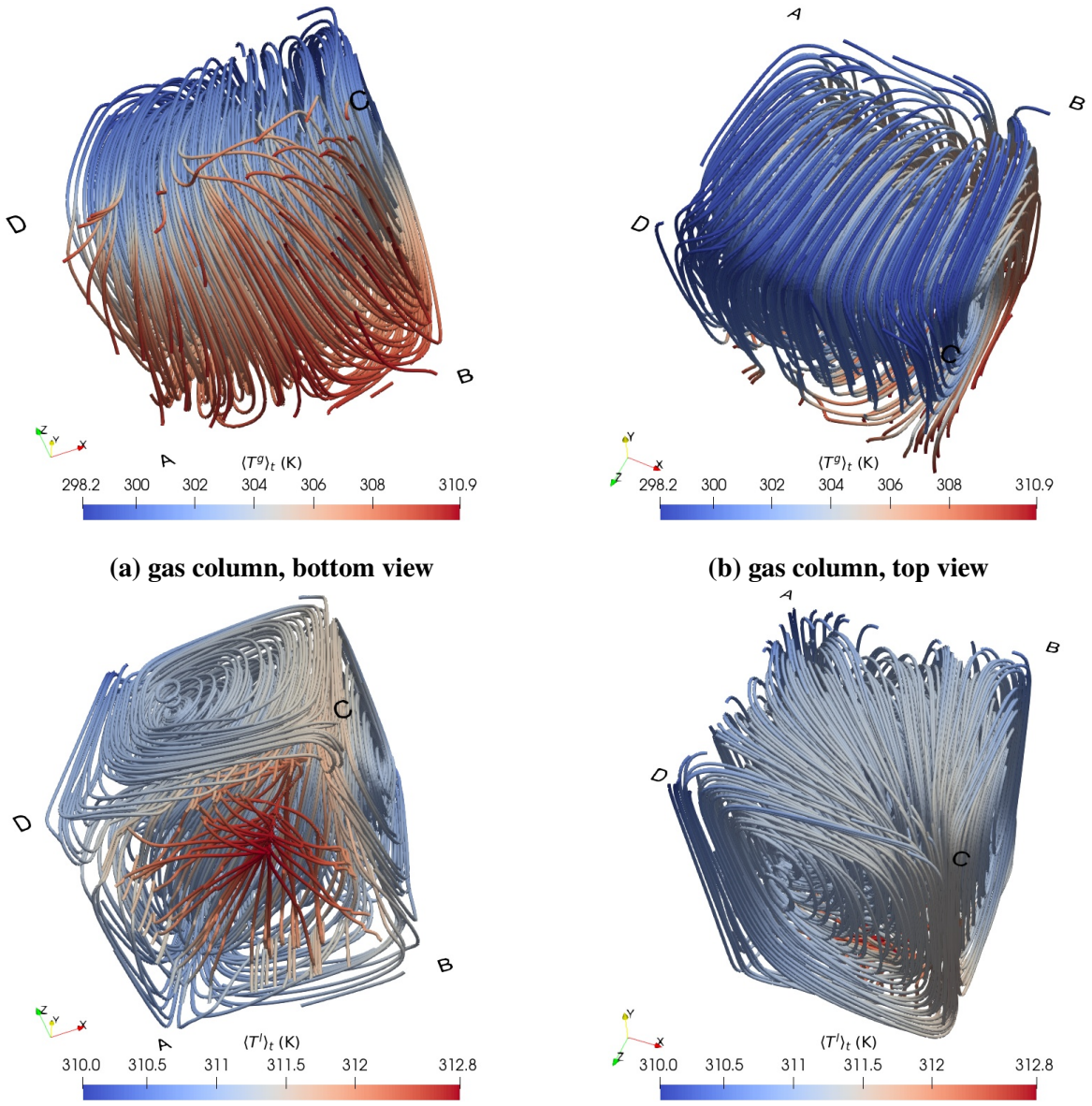
1. Case 1

Plots of time-averaged streamlines in these regions, colored with temperature, are presented in Fig. 4. They show that the flow in the gas column is organized in a single large roll aligned with one of the vertical faces of the cavity. Such a flow structure is typical for laminar thermal convection[21,62].

Actually, it is well known that, over a large range of Rayleigh numbers, thermal convection is organized in a large convective structure, referred to as Large Scale Circulation (LSC) or mean wind; see for example[63] for RBC and[14,16] for convection in cavities. The LSC can be composed of one or multiple rolls, depending on the Rayleigh number and the geometry of the flow domain. The singe roll shown in Figs. 4a and 4b is the LSC in the gas column. It is worth adding that the LSC fluctuates slightly with time due to its interaction with the convective structures of the water at the free surface. However, these fluctuations are small and too weak to modify the established flow pattern.

With regard to the water column (Fig. 4d), the flow above the porous medium is also organized in a single-roll LSC. This is aligned with the diagonal plane 1, with the ascending plume located at edge C and the descending one at edge A. Additionally, we can identify two other descending plumes (currents) of cold water at edges B and D. In other words, at the edges there are three descending plumes and an ascending one. As it can be observed in Fig. 4c, once the descending plumes reach the bottom wall, they do not enter the porous medium but move around it while their temperature increases. Eventually, they merge and form the ascending plume of hot water in the vicinity of edge C.

The streamlines inside the porous medium (Fig. 4c) are quite sparse, which indicates weak horizontal motion from its borders towards the diagonal plane 1 (which is also the plane of



(a) gas column, bottom view

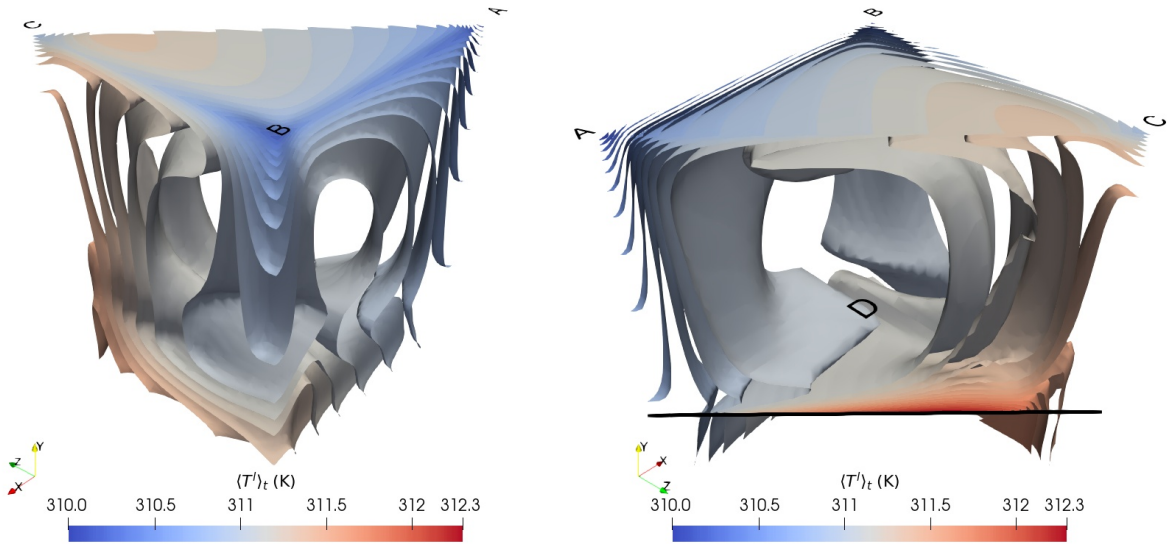
(b) gas column, top view

(c) water column, bottom view

(d) water column, top view

FIG. 4. Case 1: top and bottom views of time-averaged streamlines in the water and gas columns. The streamlines are colored by the time-averaged temperature. The letters A, B, C and D refer to the four edges of the cuboid.

alignment of the LSC above). Near the border of the porous medium and close to the edge C, the streamlines become intertwined which implies vertical motion. More specifically, these are streamlines of ascending hot water inside the porous medium but close to its walls. In other words, this weak ascending motion inside the porous medium is adjacent to the ascending plume along the edge C. Overall, inside the porous medium, the water neighboring the descending plumes is colder than the water neighboring the ascending one. This is to be expected because the heating provided



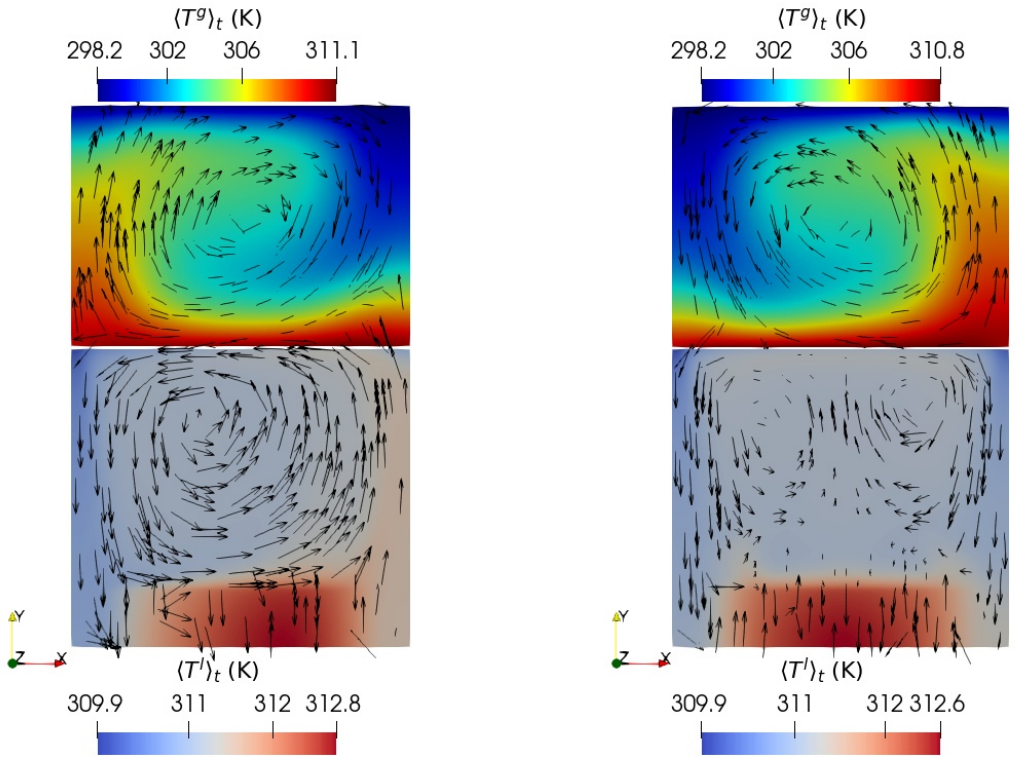
(a) outside vew **(b) inside view**

FIG. 5. Case 1: temperature iso-surfaces of temperature. For visibility purposes, the iso-surfaces inside the porous medium are excluded. The horizontal black line on the right marks the horizontal border of the porous medium, i.e. the level $y = h_p$.

by the solid matrix is uniform and does not introduce any bias on the temperature variations in the horizontal direction.

In order to gain additional insight on the convective patterns and heat transport, we have plotted temperature iso-surfaces in Fig. 5. These plots confirm the presence of 3 descending plumes (at edges A, B and D) and an ascending one at edge C in the water column. These plumes and the LSC are the principal mechanisms for heat transport in the water above the porous medium. We further infer (from Fig. 5 but also from Fig. 6 below) that once a descending plume reaches the porous medium, at $y = h_p$, it splits into two parts. The principal part continues the descent and eventually moves around the porous medium. While the second turns by 90° and moves horizontally right above the porous medium, thereby becoming warmer. Eventually, a warm horizontal current is formed right above the porous medium (which in fact is part of the LSC of the pure-water region) that joins the ascending plume at edge C.

In Fig. 6 we present color plots of the time-averaged temperature field at the two diagonal planes, superimposed with plots of the (time-averaged) velocity vectors. It is noted that the depicted vectors are actually projections of the normalized (unity) velocity vectors on the corresponding diagonal plane. As such, their apparent length is indicative of the alignment of the velocity vector to that plane.

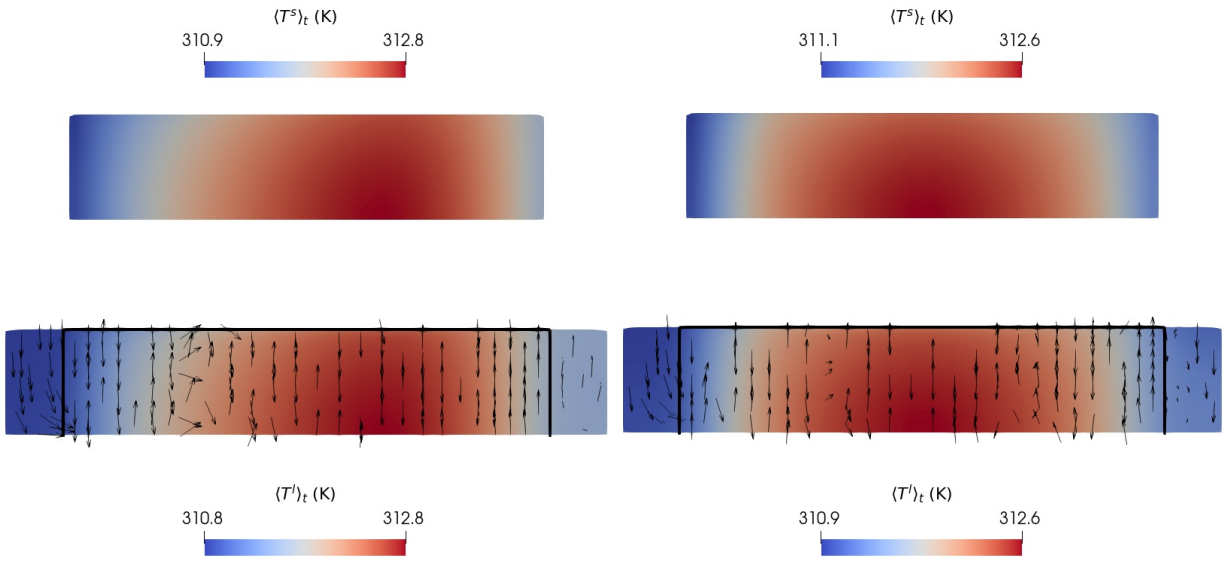


(a) diag. 1 **(b) diag. 2**

FIG. 6. Case 1: color plots of the time-averaged temperature and superimposed vector plots of the time-averaged velocity. (a) diagonal plane 1 (AC), (b) diagonal plane 2 (BD). Since the free surface descends, the layers of cells in which the free surface was located have not been taken into account in time averaging and are thus removed from the plots. For better visibility, different color maps are used for the water and gas columns. The depicted vectors are projections of the normalized (unity) velocity vectors on the diagonal planes.

These plots confirm the development of a single-roll LSC in the gas that is aligned with one of the vertical faces of the cuboid. Accordingly, the temperature distribution and fluid motion in the two diagonal planes are symmetric to one another. As mentioned above, this is typical of thermal convection in the laminar regime. Further, in these plots we clearly identify a single-roll LSC in the water (aligned with the diagonal plane 1), three descending plumes and one ascending one at the edges of the domain. By comparisons there is lesser amount of water that moves through the borders of the porous medium, which implies low horizontal circulation therein. In fact, inside the porous medium, the most prominent pattern appears to be simply vertical motion of water.

To analyze this issue further, in Fig. 7 we present plots of $\langle T^l \rangle_t$ and $\langle T^s \rangle_t$, superimposed with velocity vectors, at the two diagonal planes of the porous-medium region. These plots confirm



(a) diagonal plane 1 **(b) diagonal plane 2**

FIG. 7. Case 1: color plots of the time-averaged temperature of the solid matrix and liquid water, superimposed with time-averaged velocity vector plots. Top: $\langle T^s \rangle_t$. Bottom: $\langle T^l \rangle_t$.

that in the bulk of the porous medium, the fluid moves vertically. It is also interesting to observe that even though the solid matrix emits heat uniformly, its temperature varies considerably in the horizontal directions. More specifically, the temperature near the vertical borders is lower than in the bulk. This is to be expected since those borders are close to the descending plumes which carry water at low temperatures. Such a phenomenon had also been reported in[36] and is attributed to the water circulation around the porous medium. Actually, this circulation enhances convective heat transport in the pure-water region above and makes it more intense than in the corresponding RBC. On the other hand, the temperature variations in the vertical direction are much attenuated. In other words, inside the porous medium, the temperature gradient is essentially normal to the velocity vector, which implies weak convective transport therein. It is also interesting to note that, overall, the two phasial temperatures are close to each other, which is indicative of efficient heat transfer from the solid matrix to the interstitial fluid during the transient stage of the flow.

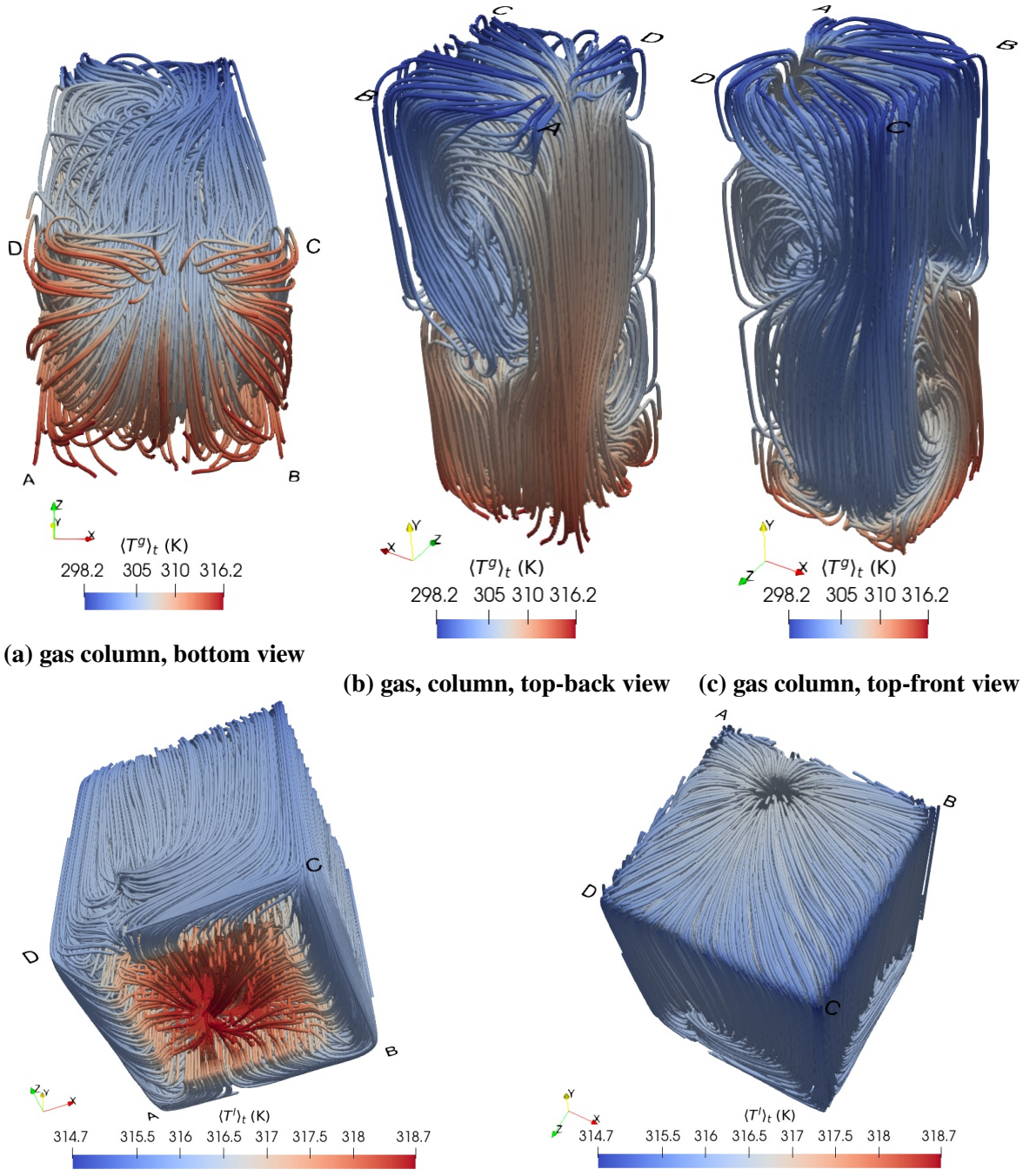
Finally, it is noted that, as in[21], the distribution of vapor mass fraction in the gas column, Y_v, is very close to that of the temperature. This is to be expected because the Lewis number is close to unity, $Le^g = 0.82$.

2. Case 2

Next, we discuss the flow patterns and convective structures in case 2. In Fig. 8, we present top and bottom views of time-averaged streamlines in the two fluid columns. In the gas, the flow is organized in a dual-roll circulation pattern. The two rolls are superimposed, i.e. one lies on top of the other. Further they are aligned with vertical faces of the cavity that are perpendicular to each other: the bottom roll is aligned with the face normal to the z-axis, and the top one with the face normal to the x-axis. Additionally, there is an ascending plume along edge A and a descending one along edge C. These two currents span the height of the gas column, thereby forming a roll of outer circulation. This flow organization has also been observed in earlier simulations of ours of thermal convection in air-water systems without immersed porous medium[21]. It is also interesting to observe in Fig. 8a that the descending gas of the bottom roll impinges the water's free surface at a point that is located close to the face of the cavity and halfway between edges D and C.

In the water column, the flow is organized in a single-roll LSC aligned with the diagonal plane 1, as it can be seen in Fig. 8e. This LSC impinges upon the free surface at a point close to edge A. Also, from the bottom view of Fig. 8d, we can observe streamlines of cold water entering the porous medium. In fact, once a descending plume reaches the bottom wall it splits into two streams; one moves around the porous medium and the other one enters it. The fact that in the bottom view the streamlines inside the porous medium are denser than in case 1 implies strong horizontal circulation therein. On the contrary, in case 1, there was comparatively little fluid motion towards the porous medium. This difference is attributed to the fact that in case 2 the Rayleigh number is higher and, therefore, convective motions are stronger. As a result, the descending cold fluid in the bottom part of the domain has enough momentum to counterbalance interphasial drag and enter the porous medium. Inside the porous medium itself, we can observe a horizontal motion of water from the edges towards the bulk of the solid matrix. Nonetheless, in the bulk, water essentially ascends vertically.

To get more insight on the mechanisms of heat transport, we present plots of temperature iso-surfaces in Fig. 9. We observe that in the water, the plumes at all four edges are descending (whereas in the previous case three plumes were descending and one was ascending). In other words, cold water is brought down from the free surface along all the edges of the cavity. As already explained, once these plumes reach the bottom wall, they split and one part moves around the porous medium and the other part enters it. Right above the horizontal porous interface, the



(a) gas column, bottom view

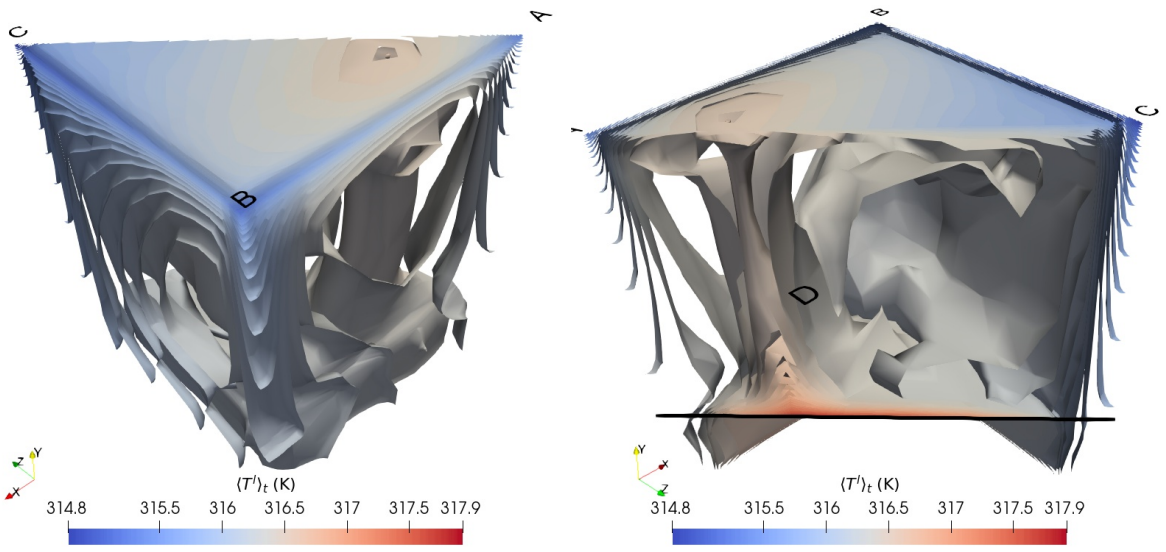
(b) gas, column, top-back view

(c) gas column, top-front view

(d) water column, bottom view

(e) water column, top view

FIG. 8. Case 2: top and bottom views of the time-averaged streamlines in the water and gas columns. The streamlines are colored by the value of the time-averaged temperature. The letters A, B, C and D refer to the four corners of the domain. (a) gas column, bottom view. (b) gas column, top-back view. (c) gas column, top-front view. (d) water column, bottom view. (e) water column, top view.



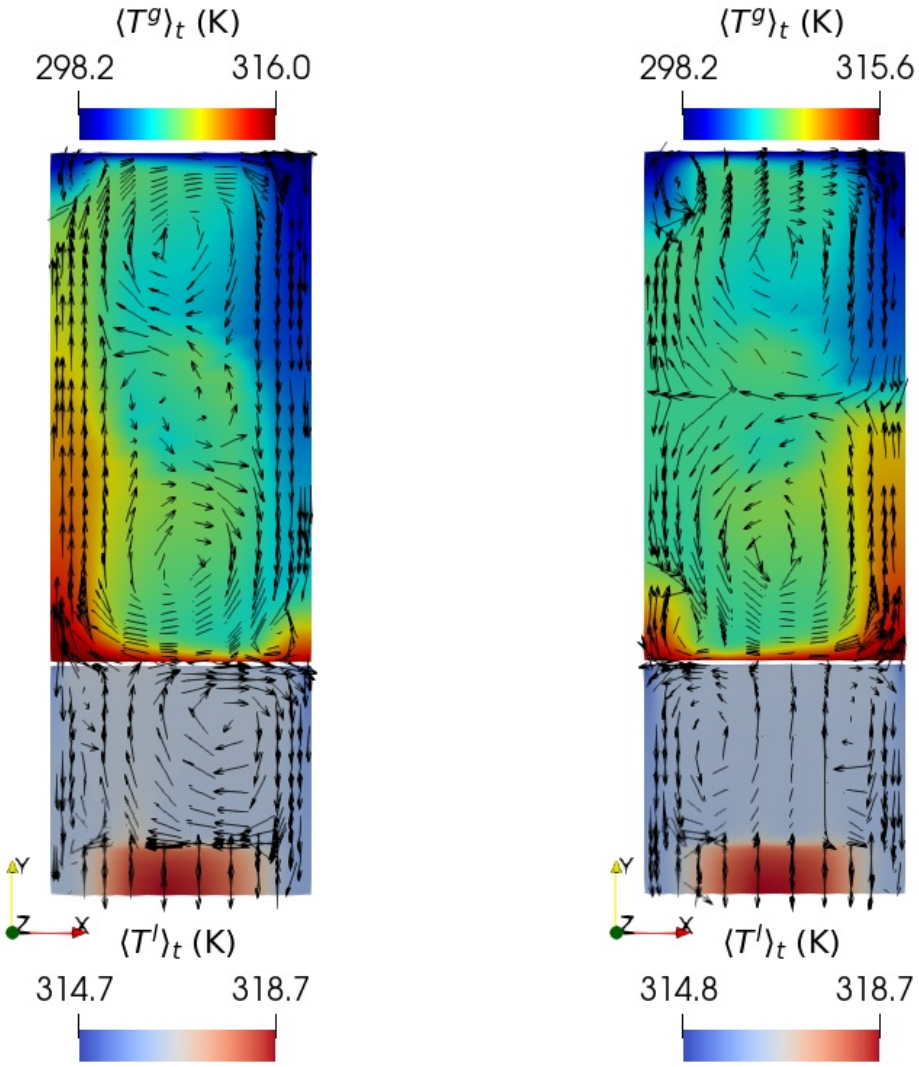
(a) outside view **(b) inside view**

FIG. 9. Case 2: temperature iso-surfaces of temperature. For visibility purposes, the iso-surfaces inside the porous medium are excluded. The horizontal black line on the right marks the horizontal border of the porous medium, i.e the level $y = h_p$.

water that exits the porous medium eventually joins the ascending plume of the LSC located in the diagonal plane 1 and at approximately one third of the diagonal width, close to A. Thus, in the bottom region, the main heat-transfer mechanisms are interphasial heat exchange inside the porous medium between and convection in its outskirts. Whereas in the pure-water region above, the main mechanism is heat convection via the LSC which brings ascending warm water to the free surface and via the descending plumes at the edges.

These findings are further corroborated by the color plots of the time-averaged temperatures at the two diagonal planes, shown in Fig. 10. These plots clearly depict a dual-roll LSC in the gas column aligned with the diagonal plane 2. At mid-height of the gas column, a region with a strong shear marks the transition from the lower roll to the upper one. Further, we can observe the development of an outer roll aligned with the diagonal plane 1 that spans the height of the gas column. Overall, the flow organization resembles the one that was predicted in our earlier simulations of convection in air-water systems heated uniformly by the bottom wall[21].

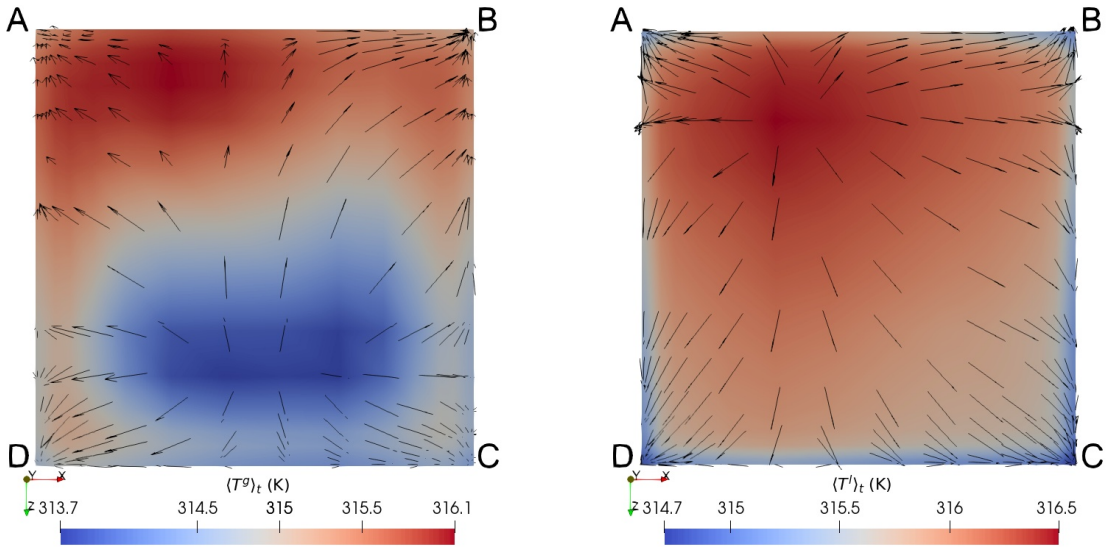
In the same figure, we can also observe the development of a single-roll LSC in the water above the porous medium. This is aligned with the diagonal plane 1. The four descending plumes at the edges of the cavity are also clearly visible. They start at the free surface and terminate at the bottom wall.



(a) diag. 1 **(b) diag. 2**

FIG. 10. Case 2: color plots of the time-averaged temperature and superimposed vector plots of the time-averaged velocity. (a) diagonal plane 1, (b) diagonal plane 2. Since the free surface descends, the layers of cells in which the free surface was located have not been taken into account in time averaging and are thus removed from the plots. For better visibility, different color maps are used for the water and gas columns. The depicted vectors are projections of the normalized (unity) velocity vectors on the diagonal planes.

Next, we examine the flow patterns in the vicinity of the free surface. To this end, in Fig. 11, we provide color plots of the time-averaged temperature (superimposed with velocity vector-plots) slightly above and below the free surface. In these plots, we can discern the horizontal currents at the two sides of the free surface, which are part of the corresponding LSC. On the gas side, the fluid moves from the face DC to the face AB, whereas on the water side it has the opposite



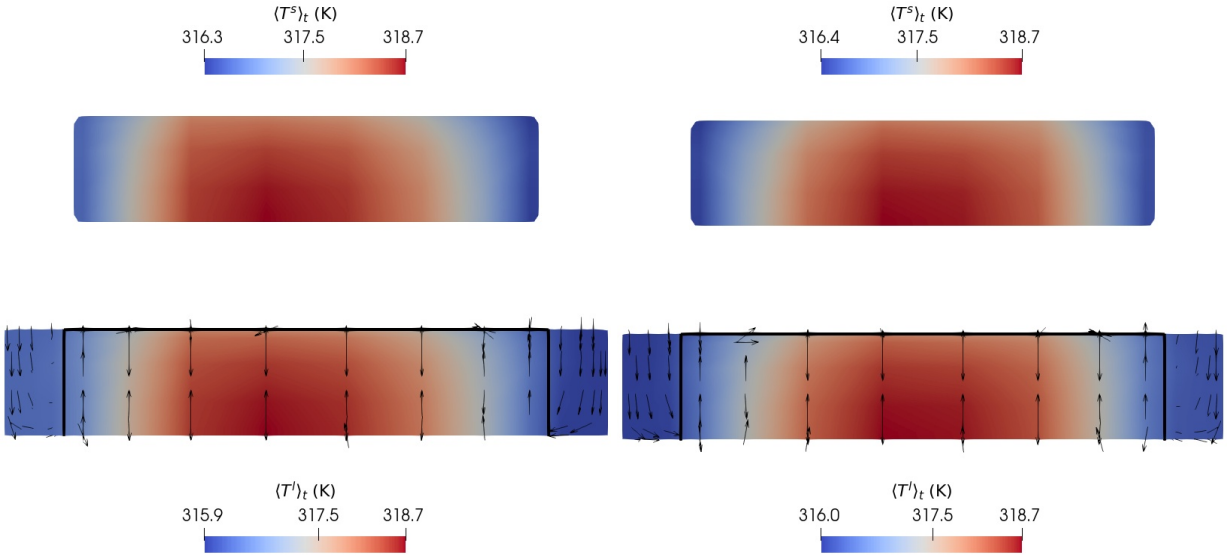
(a) above the free surface ($y = 1.01h_0$) **(b) below the free surface** ($y = 0.99h_0$)

FIG. 11. Case 2: time-averaged color plots of the temperature, superimposed with velocity vector plots, slightly above and below the free surface.

direction. This is due to the fact that the lower roll of the LSC in the gas and the LSC in the water have the same direction of rotation, i.e. they are co-rotating. For this reason, they impinge upon the free surface at different points: the impingement point on the gas side close to the face DC and that on the water side is close to the face AB.

Additionally, on the gas side there is a stagnation point that coincides with the impingement point on the water side. Evidently, this is also a hot spot, since it is in contact with the ascending plume of high-temperature water. Its presence is explained by the fact that impingement points are characterized by minima of horizontal velocities and shear stresses. Then, by continuity of those variables according to (27), the impingement point of the current with the high inertia (water side) induces a stagnation point on the other side of the free surface (gas side). This feature suggests a coupling between the main convective rolls at the two sides of the free surface. More specifically, the main convective roll in the water influences the dynamics of the LSC in the gas. A similar phenomenon was also predicted earlier in simulations of convection in air-water systems[21,22]. Therein, however, the main convective rolls were counter-rotating and, therefore, the impingement points on the two sides of the free surface were close to each other.

Finally, in Fig. 12 we present color plots of the time-averaged phasial temperatures in the porous-medium region. From these plots we infer that, as in case 1, $\langle T^l \rangle_t$ and $\langle T^s \rangle_t$ are close to one another. Outside the porous medium, the dominant feature is the descending plume of cold



(a) diagonal plane 1 **(b) diagonal plane 2**

FIG. 12. Case 2: color plots of the time-averaged temperature of the solid matrix and liquid water, superimposed with time-averaged velocity vector plots. Top: $\langle T^s \rangle_t$. Bottom: $\langle T^l \rangle_t$.

water. Inside the porous medium, the phasial temperatures are lower near its vertical borders; this is explained by the fact they are neighboring the descending plumes. However, the temperatures increase towards the centerline of the cuboid. The vector plots reaffirm that the fluid motion in the bulk of the porous medium is mostly vertical. Eventually, water exits the porous medium from the horizontal border (located at the plane $y = h_p$) and then joins the ascending branch of the LSC.

C. Flow statistics

In this section, we present results for global quantities and the flow statistics in the two columns. In Fig. 13 we have plotted the evolution of the area-averaged temperature at the free surface, $\langle T_F \rangle_{xz}$. We observe that in case 1 $\langle T_F \rangle_{xz}$ is stabilized but exhibits small-amplitude, low-frequency oscillations. This was also the case in the transient stage, i.e. during the development of the flow. As mentioned above, these single-frequency oscillations are characteristic of thermal convection in the transitional regime (as is the case in the water column)[61]. Further, in case 2, the free-surface temperature is also stabilized but exhibits random oscillations of very small amplitude and higher frequency. As mentioned above, these oscillations are attributed to the flow turbulence.

Next, in Fig. 14 we present the evolution of the area-averaged evaporative mass flux $\langle \dot{m}'' \rangle_{xz}$ and the free-surface height h. We see that in both cases $\langle \dot{m}'' \rangle_{xz}$ varies in the same manner as $\langle T_F \rangle_{xz}$. In

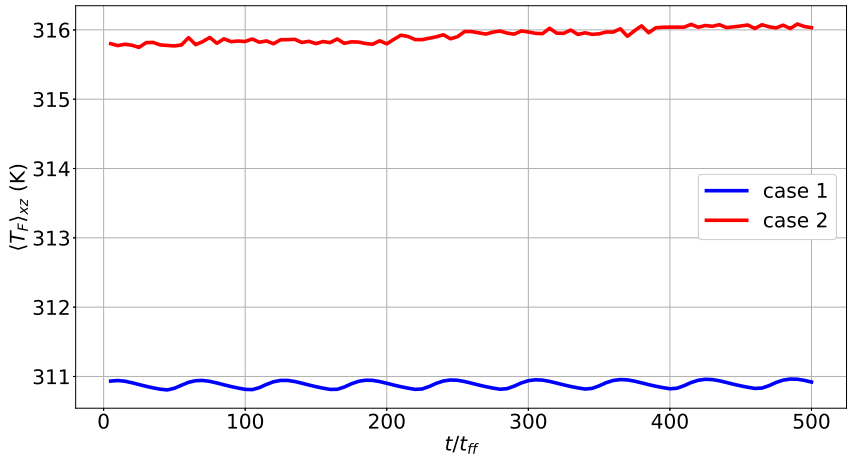


FIG. 13. Evolution of the area-averaged free-surface temperature $\langle T_F \rangle_{xz}$.

case 1 it oscillates in the same low frequency, and in case 2 it exhibits the same random fluctuations as does the temperature. This is because changes in the temperature make vary the gas properties which control the evaporation rate, such as density and vapor concentration as per Eq. (25). Then, as $\langle T_F \rangle_{xz}$ varies, so does $\langle \dot{m}'' \rangle_{xz}$. Nonetheless, the fluctuations of the evaporative flux are very small and, therefore, the rate of descent of the free surface remains almost constant. This is readily confirmed from the profile of h in Fig. 14, which is almost linear. It is clarified that in Fig. 14 the profile of h in case 2 is located below that in case 1 due to different reference lengths; in absolute terms h drops faster in case 2 due to higher evaporative flux.

It is also worth adding that the computed free-surface temperature is very close to the estimated one. For this reason, the computed Rayleigh numbers in the two columns are satisfactorily close to those estimated initially. Crucially, the computed Rayleigh numbers are such that the grid resolution criteria mentioned above remain satisfied. For completion purposes, in Table VI we provide the computed values of the mean temperature at the three significant planes (bottom wall, free surface, and top border of the porous medium), together with the computed values of the Rayleigh numbers and evaporative flux.

We further note that, according to the plots of Figs. 13 and 14, the oscillation frequencies of $\langle T_F \rangle_{xz}$ and $\langle \dot{m}'' \rangle_{xz}$ are considerably higher than those derived from the plots of the transition stage in Fig. 3. The reason for this divergence is that the plots in these figures were generated using a higher sampling rate of the data, namely, one data point per 5 t_{ff}. Whereas the plots in Fig. 3 were generated using one data point every 50 t_{ff}. This in turn implies that the actual oscillation

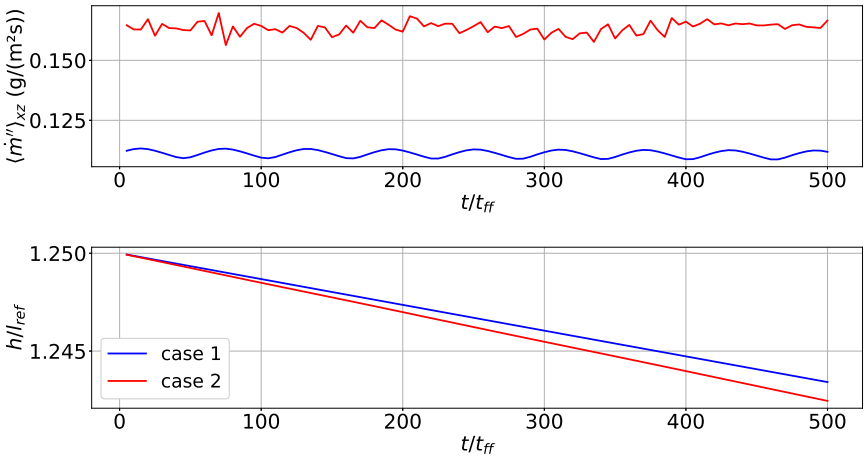


FIG. 14. Top: evolution of the evaporative mass flux $\langle \dot{m}'' \rangle_{xz}$. Bottom: evolution of the height of the water's free surface.

TABLE VI. Computed values of mean temperatures, temperature differences, Rayleigh numbers and evaporative mass flux.

	$\langle T_F \rangle$	$\langle T_p \rangle$	$\langle T_h \rangle$	ΔT^l	ΔT^g	Ra^l	Ra^g	$\langle \dot{m}'' \rangle$
case 1	310.925	311.59	311.78	0.665	12.775	2.29×10^5	7.5×10^3	0.11
case 2	315.9	316.89	317.15	0.99	17.75	1.29×10^6	1.15×10^6	0.165

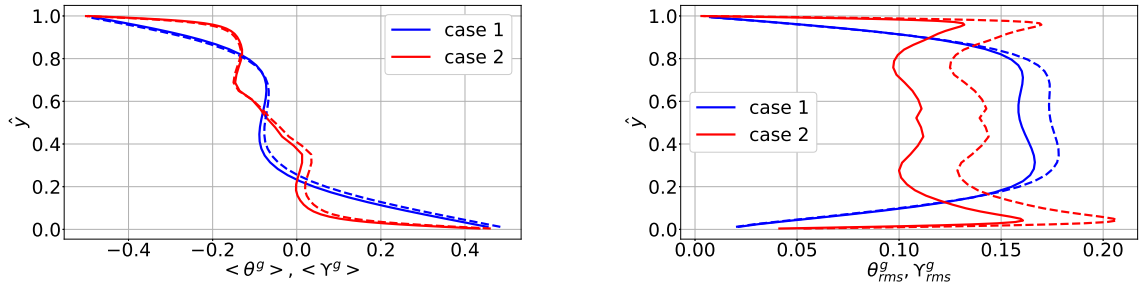
frequencies of $\langle T_F \rangle_{xz}$ and $\langle \dot{m}'' \rangle_{xz}$ are those that are inferred from the plots in Figs. 13 and 14.

We proceed to discuss the first and second-order statistics of normalized phasial temperatures, θ^l and θ^g, and normalized vapor mass fraction Υ^g. These variables are defined as follows,

$$\theta^g = \frac{T^g - T^g_{ref}}{\langle T_F \rangle - T_c}, \qquad \theta^l = \frac{T^l - T^l_{ref}}{\langle T_p \rangle - \langle T_F \rangle}, \qquad \Upsilon^g = \frac{Y_v - \frac{\langle Y_{v,F} \rangle + Y_v^{amb}}{2}}{\langle Y_{v,F} \rangle - Y_v^{amb}}. \tag{46}$$

It is clarified that θ^l is defined in the pure-water region ($h_p < y < h$) and not in the entire water column.

In Fig. 15, we have plotted the profiles of the mean and rms values of θ^g and Υ^g; the term 'rms' refers to the root mean square of the fluctuations of area (xz) and time averaged value. In case 1, the mean profiles take a reverted S shape, as is commonly the case in laminar thermal convection[21,62]. This shape is characteristics of flows organized in a single convective roll. Also, according to our simulations, the rms profiles are not zero but adopt a "double well" shape. In other words, the variations are higher in the bulk of the column, in which they exhibit two local peaks, but decrease



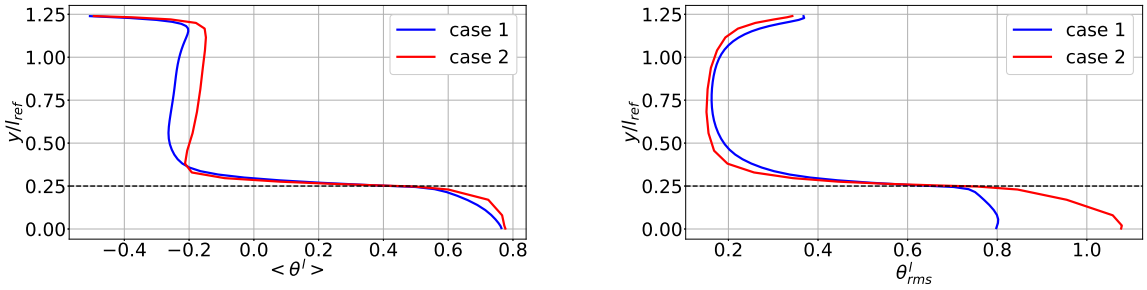
(a) gas column, mean profiles **(b) gas column, rms profiles**

FIG. 15. Mean and rms profiles of normalized temperature (solid lines) and vapor mass fraction (dashed lines) in the gas column. (a) $\langle\theta^g\rangle$ and $\langle\Upsilon^g\rangle$. (b) θ^g_{rms} and Υ^g_{rms}.

steeply near the column boundaries, as is typical in laminar natural convection[62]. We further note that the profiles of $\langle\theta^g\rangle$ and $\langle\Upsilon^g\rangle$ are close to each other, which is due to the fact that the Lewis number of air is close to unity. The same holds true for the corresponding rms profiles too.

Also in Fig. 15, we observe that in case 2 the profile of $\langle\theta^g\rangle$ is no longer a reversed S but resembles two reversed S on top of each other. This implies the presence of a local minimum and a local maximum in the bulk. Evidently, this is due to the fact that the flow is now organized in a dual-roll convective structure with one roll on top of the other. Further, the rms profiles are characteristic of convection in the transitional/soft turbulence regime, with peaks at the edges of the boundary layers and lower values in the bulk. It is also interesting to observe that while the profiles of $\langle\theta^g\rangle$ and $\langle\Upsilon^g\rangle$ are close as expected, this is no longer the case for the corresponding rms profiles. This divergence is a numerical artifact and attributed to the coarseness of the LES grid which yields less accurate 2nd-order statistics in the bulk of the domain.

With regard to the water column, plots of the mean and rms profiles of the normalized temperature, θ^l, are presented in Fig. 16. In both cases (1 and 2), the mean temperature decreases monotonically with height in the porous-medium region. Further, it exhibits steep gradients in the vicinity of the plane $y = h_p$, i.e. at the level of the horizontal porous-pure water interface. In the pure-water region above, $\langle\theta^l\rangle$ adopts a Z profile, with strong negative gradients near the boundaries and mild positive gradients in the bulk. Also, the rms of the thermal fluctuations in the porous-medium region decrease with height and drop sharply in the bulk of the pure-water region. The small values therein imply efficient thermal mixing and are typical of turbulent thermal convection. Once the rms profile attains its minimum (close to mid-height of the pure-water region), it increases and gets maximized at the free surface. This peak is a manifestation of the



(a) water column, mean profiles **(b) water column, rms profiles**

FIG. 16. Mean and rms profiles of the temperature in the water column for case 1 and case 2. (a) $\langle\theta^l\rangle$. (b) θ^l_{rms}.

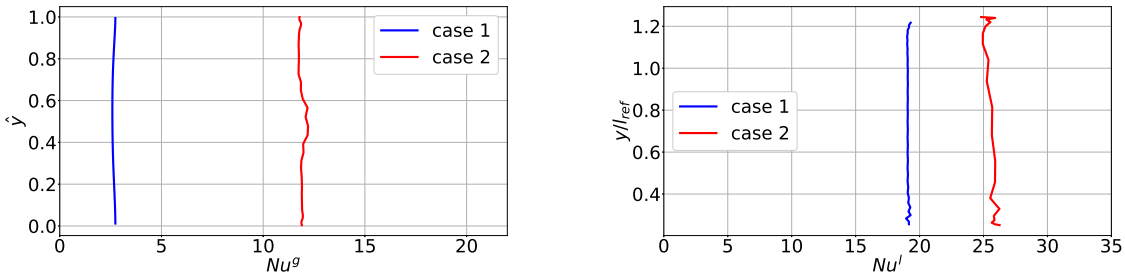
thermal boundary layer at it. It is also interesting to add that, overall, the shape of the mean and rms temperature profiles are similar to those predicted in[36] for convection in water-filled cavities heated by immersed porous media (without accounting for evaporation and the presence of air).

We now present results for the local Nusselt number in the pure-water region and the gas column, $Nu^l(y)$ and $Nu^g(y)$ respectively. These are defined at any given horizontal plane of the respective subdomains as follows

$$Nu^l(y) = \frac{\langle \rho^l c_p^l\, v^l\, T^l\rangle - \langle \lambda^l \frac{\partial T^l}{\partial y}\rangle}{\lambda^l \frac{\Delta T^l}{l_{ref}}}, \qquad Nu^g(y) = \frac{\langle \rho^g c_p^g\, v^g\, T^g\rangle - \langle \lambda^g \frac{\partial T^g}{\partial y}\rangle}{\lambda^g \frac{\Delta T^g}{H-h_0}}. \tag{47}$$

Once the flow is fully developed and becomes statistically stationary, $Nu^g(y)$ and $Nu^l(y)$ should be constant and equal to the so-called global Nusselt number. Their profiles are plotted in Fig. 17. We observe that, in both cases, they are almost constant as expected. Any deviation from a vertical straight line is attributed to numerical errors. These errors are more pronounced in case 2 due to the coarseness of the LES grid. In particular, $Nu^l(y)$ exhibits some oscillations near the boundaries while $Nu^g(y)$ has a small peak in the bulk. These numerical artifacts are well documented in LES of turbulent thermal convection[17,50]. It is also worth recalling that formally the system is not at steady state because the water level decreases due to evaporation. In principle, this also contributes to the deviation of the profile from a straight line. Nonetheless, the time scale of evaporation is quite long and, therefore, the deviation caused by this phenomenon is expected to be very small.

We further observe that the Nusselt number increases considerably with the Rayleigh number, as expected. Overall, in the pure-water region, Nu^l is significantly higher than if the heat supply had come from the bottom wall (as was the case in[21]). Indeed, in the problem in hand, the water column is heated in a non-uniform manner. This enhances the circulation of the water and the



(a) gas column **(b) pure-water region**

FIG. 17. Profiles of the local Nusselt numbers.

convective transport, which is manifested by significantly higher Nusselt numbers. On the other hand, the values of the Nusselt number in the gas column are quite close to those of our earlier study[21] that did not involve an immersed porous medium.

Finally, we provide results for the local Sherwood in the gas column, $Sh^g(y)$, which is a measure of the strength of convective mass transport with respect to the diffusive one,

$$Sh^g(y) = \frac{\langle \rho^g \, v^g \, Y_v \rangle - \langle \rho^g \mathcal{D} \frac{\partial Y_v}{\partial y} \rangle}{\rho^g \mathcal{D} \frac{Y_{v,F} - Y_v^{amb}}{H - h_0}}. \tag{48}$$

For fully developed flow, $Sh^g(y)$ should also be constant. The computed profiles of $Sh^g(y)$ are provided in Fig. 18. These are indeed constant, as expected, with the exception of some small variations in case 2. Actually, the value of the ratio $Sh^g(y)$ and $Nu^g(y)$ is reasonably close to the empirical scaling $Sh^g/Nu^g = Le^{0.25}$ proposed in[64]. In this case, $Le^{0.25} \approx 0.95$. The deviation of our numerical predictions from this scaling lies on the fact that it has been derived assuming pure thermal convection (without evaporation) and constant thermophysical properties. However, none of these assumptions are valid for the problem in hand. The computed Nusselt and Sherwood numbers are listed in Table VII.

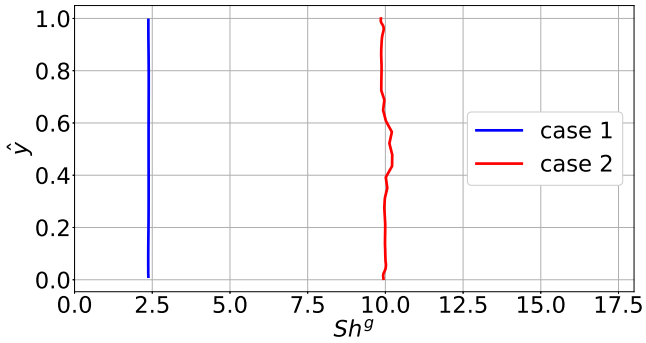


FIG. 18. Profiles of $Sh^g(y)$ in the gas column.

TABLE VII. Numerical predictions for the Nusselt and Sherwood numbers.

	Nu^l	Nu^g	Sh^g	Sh^g/Nu^g
case 1	19	2.65	2.38	0.9
case 2	25.5	11.89	9.99	0.84

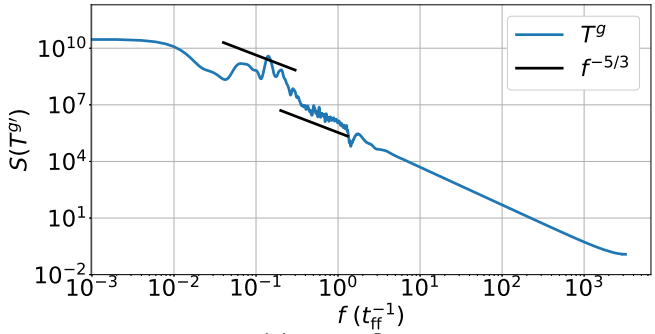
It is also worth adding that according to our simulations, the Weber number is estimated at $We = 0.025$ in case 1, and $We = 0.055$ in case 2. These small values of We justify our assumption that the free surface of the water remains flat. Also, the Marangoni number is estimated at $Ma = 25000$ in case 1, and $Ma = 84500$ in case 2. In other words, the ratio $\frac{Ma}{Ra}$ is estimated at 0.109 in case 1, and 0.065 in case 2. This in turn implies that in the water thermal convection is driven by buoyancy and thermo-capillary effects may indeed be neglected.

D. Spectral properties of the thermal fluctuations

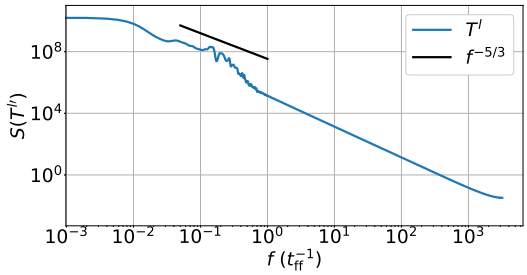
In this section, we analyze the power spectrum S of the signals of the thermal fluctuations.

$\underline{Case1}$. As mentioned above, the thermal convection in the pure-water region belongs in the transitional regime but in the gas it is laminar. Therefore, it is not particularly informative to study the spectra of the thermal fluctuations in this case. Nonetheless, we recall that the free-surface temperature oscillates at a single frequency, as it is clearly shown in Fig. 13. Actually, the frequency of oscillation is $f \approx 0.016\, t_{\rm ff}^{-1}$.

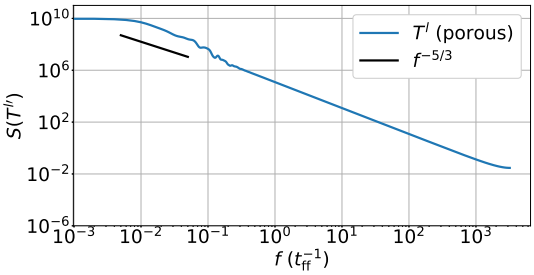
It is therefore interesting to examine if this frequency can be associated to the convective structure of the flow. To this end, and following the reasoning of[65], we compute an estimate of the time that it takes for a fluid particle to travel around the perimeter of the LSC in the pure-water region at its plane of alignment. This is a single-roll LSC and constitutes the principal convective structure below the free surface. For computational purposes, its projection at the plane of alignment can be approximated as an ellipse. According to Fig. 6, the major axis of this ellipse is the full length of the diagonal $\sqrt{2}W$, while the minor axis is the length of the pure-water region, $0.8\, h_0$. Then by computing the time and volume average of the amplitude of the velocity vector, we find that this time is equal to $62.5\, t_{\rm ff}$. This corresponds to a frequency of rotation $f \approx 0.016\, t_{\rm ff}^{-1}$, which is very close to the oscillation frequency of the free-surface temperature. We may therefore conclude that the LSC in the pure-water region causes the free-surface temperature to oscillate at



(a) gas column.



(b) pure-water region.



(c) porous-medium region.

FIG. 19. Power spectra S of the signals of the thermal fluctuations.

its characteristic frequency.

*Case*2. We have computed the power spectrum S of the signals of the thermal fluctuations at the centers of the three regions that comprise the flow domain: the porous-medium region, the pure-water region and the gas column. These points are located at the centerline of the cuboid and at $\frac{y}{l_{ref}} = 0.125$, 0.75 and 2.63 respectively. In the calculation of the spectra, the signal noise has been reduced by applying a Gaussian filter.

The plots of the (non-normalized) spectra at these locations are provided in Fig. 19. We can observe that all three spectra exhibit the same trends. For example, at very low frequencies (the initial range), they are all flat. They start to drop at approximately $f \approx 0.002\, t_{\mathrm{ff}}^{-1}$. This drop is not monotonic but subject to fluctuations. These are more pronounced in the spectrum of the gas column and much less in that of the porous region. We can also observe that in the inertial-convective subrange, the spectra drops following a power law that is equal to -5/3, as in channel flows[66] and RBC[67,68]. These common trends suggest an interaction between the flow structures in the three regions, particularly between the pure-water region and the gas column at the free surface.

It would therefore be informative to try to associate the main convective structures of the flow to specific features of the spectra. Following again the reasoning of[65], we consider the time that it takes

for a fluid particle to travel the perimeter of the LSC in the pure-water region. The perimeter can be approximated to that of an ellipse at the plane of alignment of the LSC. The major axis is equal to 0.8 of the length of the diagonal, i.e. $1.13\,W$. While its minor axis is equal to the height of the pure-water region, $l_{ref} = 0.8\,h_0$. Then the perimeter P of the LSC is estimated at $P = 3.36\,l_{ref}$. Further, according to our computations, the mean velocity amplitude is $\langle \boldsymbol{u} \rangle = 0.134 u_{\rm ff}$. This corresponds to a characteristic frequency of the LSC equal to $f = \langle \boldsymbol{u} \rangle / P = 0.04\,t_{\rm ff}^{-1}$. This frequency coincides with a local peak of the power spectra in the pure-water region and the gas column, shown in Figs. 19a and 19b. This in turn implies that the LSC in the pure-water region exerts a low-frequency modulation to the gas column. In an analogous manner, we can observe that the power spectra in the pure-water region and the gas column share another peak at $f \approx 0.15\,t_{\rm ff}^{-1}$, which is suggestive of an additional modulation of the gas from a convective structure in the water.

We further note that in the range between $f = 0.7$ and $4\ t_{\rm ff}^{-1}$ the spectrum in the gas drops in an oscillatory manner, whereas that of the pure-water region drops monotonically. In other words the spectrum in the gas has local peaks at high frequencies that are not present in the spectrum of the pure-water region. This suggests that these peaks are due to the proper dynamics of the flow turbulence in the gas. To explore this further, we consider the lower roll of the LSC in the gas column. Its perimeter is also approximated to that of an ellipse at the plane of alignment. According to Fig. 10b, its major axis is approximately 0.90 of the domain width W, which is equal to l_{ref} and its minor one equal to 0.45 of the height of the gas column $H - h_0$. Then, its perimeter is estimated at $P = 3.41\,l_{ref}$ while the mean velocity amplitude is $\langle \boldsymbol{u} \rangle = 2.96\,u_{\rm ff}$. This translates to a characteristic frequency of the LSC $f \approx 0.87\,t_{\rm ff}^{-1}$. This value is close to the local peak at $f \approx 0.8\,t_{\rm ff}^{-1}$ of the spectrum in the gas column. We thus infer that in the gas, the high-frequency peaks of the spectrum are due to the proper dynamics of the flow in the gas column. While the low-frequency ones are due to modulation from the convective structures of the pure-water region across the free surface.

It may be added that we also reproduced the power spectrum of the fluctuations of the vapor concentration in the air. As expected, it was very similar to that of the thermal fluctuations therein.

V. CONCLUSIONS

In this paper we presented a computational study of natural convection of an evaporative air-water system in a cavity heated internally by an immersed porous medium. The latter one is

assumed to consist of uniformly distributed parallel cylinders that are perpendicular to the bottom wall. Two cases were considered herein. In case 1, the flow was laminar in the air and transitional in the water. This case was treated numerical via direct numerical simulations. Whereas, in case 2, the flow was in the soft-turbulence regime both in the air and in the water. This case was treated numerical via large eddy simulations.

Overall, in both cases, the free-surface temperature and evaporation rate are essentially constant and exhibit only small fluctuations with time. Further, the immersed porous medium introduces an inhomogeneity in the heating of the water. This fact, combined with the circulation of water around and (to a lesser extent) inside the porous medium, enhances significantly the convective heat transport, as manifested by the high values of the Nusselt number in the pure-water region.

In case 1, the flow in each region is organized in a single-roll large-scale circulation. In the water, low-temperature descending plumes are established at the three edges of the cavity and an ascending plume at the fourth one. These plumes span the height of the water column. The descending ones reach the bottom wall and then move mostly around the porous medium. Also, according to our analysis, the small-amplitude thermal fluctuations at the free surface are due to the LSC in the water. In the gas, the flow is organized in a single convective cell that is aligned in the plane of one pair of lateral walls.

In case 2, the convective structure in the gas is more complex. The flow is organized in a dual-roll LSC. The two rolls are superimposed and aligned to different vertical faces of the cavity, i.e. their planes of alignment are perpendicular to each other. Additionally, there is an outer roll formed by one ascending and one descending plume that span the entire height of the gas column. In the water, the main structure is still an one-roll LSC but now descending plumes are formed in all four edges of the cavity. These plumes have now higher momentum, so that one part of them enters the porous medium which, in turn, results in comparatively higher circulation therein. The analysis of the spectra of the thermal fluctuations indicates that the convective structures in the pure-water region provide a low-frequency modulation of the flow in the air. Whereas the proper dynamics of the convective structures in the gas are associated to high-frequency peaks of its spectrum.

ACKNOWLEDGMENTS

The authors gratefully acknowledge the financial support provided by the Belgian Federal Public Service Economy under the Energy Transition Fund, project SFP-LOCA.

DECLARATION OF COMPETING INTEREST

The authors declare no conflict of interest.

DATA AVAILABILITY

The data that supports the findings of these study are available by the corresponding author upon available request.

AUTHOR CONTRIBUTION

J. Carlier: conceptualization (equal), methodology (equal), software, validation, investigation (equal), formal analysis, data curation, visualization, writing (equal).

M.V. Papalexandris: conceptualization, methodology (equal) investigation (equal), resources, writing (equal), project administration, supervision, funding acquisition.

REFERENCES

[1]E. Bodenschatz, W. Pesch, and G. Ahlers, "Recent developments in Rayleigh-Bénard convection," Annu. Rev. Fluid Mech. **32**, 709–778 (2000).

[2]G. Ahlers, S. Grossmann, and D. Lohse, "Heat transfer and large scale dynamics in turbulent Rayleigh-Bénard convection," Rev. Mod. Phys. **81**, 503–537 (2009).

[3]D. Lohse and K.-Q. Xia, "Small-scale properties of turbulent Rayleigh-Bénard convection," Ann. Rev. Fluid Mech. **42**, 335–364 (2010).

[4]D. Lohse and O. Shishkina, "Ultimate Rayleigh-Bénard turbulence," Reviews of Modern Physics **96**, 035001 (2024).

[5]S. M. Bower and J. R. Saylor, "A study of the Sherwood-Rayleigh relation for water undergoing natural convection-driven evaporation," Int. J. Heat Mass Tran. **52**, 3055–3063 (2009).

[6]A. Jodat, M. Moghiman, and M. Anbarsooz, "Experimental comparison of the ability of Dalton based and similarity theory correlations to predict water evaporation rate in different convection regimes," Heat Mass Tran. **48**, 1397–1406 (2012).

[7]N. Kumar and J. H. Arakeri, "Natural convection driven evaporation from a water surface,"

Procedia IUTAM **15**, 108–115 (2015), IUTAM Symposium on Multiphase Flows with Phase Change: Challenges and Opportunities.

[8]M. Q. Brewster, "Evaporation of water at high mass-transfer rates by natural convection air flow with application to spent-fuel pools," Int. J. Heat Mass Tran. **116**, 703–714 (2018).

[9]L. Zhang, K. L. Chong, and K.-Q. Xia, "Moisture transfer by turbulent natural convection," J. Fluid Mech. **874**, 1041–1056 (2019).

[10]J. Martin and B. Migot, "Experimental study of the surface evaporation rate of a heated water pool at high temperature using infrared thermography," 18th International Topical Meeting on Nuclear Reactor Thermal Hydraulics , 2302–2313 (American Nuclear Society, Portland, Oregon, 2019).

[11]T. Poós and E. Varju, "Review for prediction of evaporation rate at natural convection," Heat Mass Transfer **55**, 1651–1660 (2019).

[12]O. Zikanov, D. N. Slinn, and M. R. Dhanak, "Turbulent convection driven by surface cooling in shallow water," J. Fluid Mech. **464**, 81–111 (2002).

[13]W. A. Hay and M. V. Papalexandris, "Numerical simulations of turbulent thermal convection with a free-slip upper boundary," Proc. Roy. Soc. A-Math. Phys. **475**, 20190601 (2019).

[14]J. Marichal and M. V. Papalexandris, "On the dynamics of the large scale circulation in turbulent convection with a free-slip upper boundary," Int. J. Heat Mass Tran. **183C**, 122220 (2022).

[15]W. A. Hay and M. V. Papalexandris, "Evaporation-driven turbulent convection in water pools," J. Fluid Mech. **904**, A14 (2020).

[16]W. A. Hay, J. Martin, B. Migot, and M. V. Papalexandris, "Turbulent thermal convection driven by free-surface evaporation in cuboidal domains of different aspect ratios," Phys. Fluids **33**, 015104 (2021).

[17]L. Ceresiat and M. V. Papalexandris, "Numerical study of turbulent natural convection with a descending free surface due to evaporation," Flow Turbul. Combust. **115**, 469–494 (2025).

[18]H.-R. Liu, K. L. Chong, C. S. Ng, R. Verzicco, and D. Lohse, "Enhancing heat transport in multiphase Rayleigh-Bénard turbulence by changing the plate-liquid contact angles," J. Fluid Mech. **933**, R1 (2022).

[19]A. D. Demou, N. Scapin, M. Crialesi-Esposito, P. Costa, F. Spiga, and L. Brandt, "Effects of Rayleigh and Weber numbers on two-layer turbulent Rayleigh-Bénard convection," J. Fluid Mech. **996**, A23 (2024).

[20]N. Scapin, A. D. Demou, and L. Brandt, "Evaporating Rayleigh–Bénard convection: prediction

of interface temperature and global heat transfer modulation," J. Fluid Mech. **957**, A12 (2023).

[21]J. Carlier and M. V. Papalexandris, "Turbulent natural convection in an air-water system with evaporation across the free surface," Int. J. Multiphas. Flow **177**, 104873 (2024).

[22]J. Carlier, B. Podvin, and M. V. Papalexandris, "Proper orthogonal decomposition analysis of turbulent natural convection in an air–water system with evaporation across the free surface," Int. J. Multiphas. Flow **190**, 105273 (2025).

[23]L. Huguet, T. Alboussiere, M. I. Bergman, R. Deguen, S. Labrosse, and G. Lesœur, "Structure of a mushy layer under hypergravity with implications for Earth's inner core," Geophys. J. Intl. **204**, 1729–1755 (2016).

[24]J. A. Ochoa-Tapia and S. Whitaker, "Momentum transfer at the boundary between a porous medium and a homogeneous fluid-I. Theoretical development," Int. J. Heat Mass Tran. **38**, 2635–2646 (1995).

[25]S. C. Hirata, B. Goyeau, D. Gobin, M. Carr, and R. M. Cotta, "Linear stability of natural convection in superposed fluid and porous layers: influence of the interfacial modelling," Int. J. Heat Mass Tran. **50**, 1356–1367 (2007).

[26]A. d'Hueppe, M. Chandesris, D. Jamet, and B. Goyeau, "Boundary conditions at a fluid–porous interface for a convective heat transfer problem: analysis of the jump relations," Int. J. Heat Mass Tran. **54**, 3683–3693 (2011).

[27]A. d'Hueppe, M. Chandesris, D. Jamet, and B. Goyeau, "Coupling a two-temperature model and a one-temperature model at a fluid-porous interface," Int. J. Heat Mass Tran. **55**, 2510–2523 (2012).

[28]D. A. Nield and A. Bejan, *Convection in Porous Media* (Springer, 2017) 5th edition.

[29]K. Vafai, *Handbook of Porous Media* (CRC Press, 2015).

[30]P. Zhao and C. F. Chen, "Stability analysis of double-diffusive convection in superposed fluid and porous layers using a one-equation model," Int. J. Heat Mass Tran. **44**, 4625–4633 (2001).

[31]P. D. Antoniadis and M. V. Papalexandris, "Dynamics of shear layers at the interface of a highly porous medium and a pure fluid," Phys. Fluids **27**, 014104 (2015).

[32]M. Papalexandris and P. D. Antoniadis, "A thermo-mechanical model for flows in superposed porous and fluid layers with interphasial heat and mass exchange," Int. J. Heat Mass Tran. **88**, 42–54 (2015).

[33]T. Le Reun and D. Hewitt, "High-Rayleigh-number convection in porous–fluid layers," J. Fluid Mech. **920**, A35 (2021).

[34]B. Straughan, *Stability and Wave Motion in Porous Media*, Vol. 165 (Springer Science & Business Media, 2008).

[35]S. C. Cowin, *Continuum Mechanics of Anisotropic Materials* (Springer Science & Business Media, 2013).

[36]V. Hamtiaux and M. V. Papalexandris, "Turbulent thermal convection in mixed porous-pure fluid domains," J. Fluid Mech. **961**, A27 (2023).

[37]A. Bagchi and F. A. Kulacki, "Natural convection in fluid–superposed porous layers heated locally from below," Int. J. Heat Mass Tran. **54**, 3672–3682 (2011).

[38]P. D. Antoniadis and M. V. Papalexandris, "Numerical study of unsteady, thermally-stratified shear flows in superposed porous and pure-fluid domains," Int. J. Heat Mass Tran. **96**, 643–659 (2016).

[39]M. V. Papalexandris, "Thermal boundary-layer solutions for forced convection in a porous domain above a flat plate," J. Eng. Math. **144**, 3 (2024).

[40]J. Carlier and M. V. Papalexandris, "An efficient tracking method of evaporative and flat free surfaces for turbulent convection," Comput. Fluids **257**, 105882 (2023).

[41]M. V. Papalexandris, "On the applicability of Stokes' hypothesis to low-Mach-number flows," Continuum Mech. Therm. **32**, 1245–1249 (2020).

[42]T. R. Marrero and E. A. Mason, "Gaseous diffusion coefficients," J. Phys. Chem **1**, 3–118 (1972).

[43]E. W. Lemmon, M. L. Huber, and M. O. McLinden, "Standard reference database 23: reference fluid thermodynamic and transport properties," Tech. Rep. (NIST, 2010) REFPROP, 9th edition.

[44]D. L. Koch and A. J. C. Ladd, "Moderate Reynolds number flows through periodic and random arrays of aligned cylinders," J. Fluid Mech. **349**, 31–66 (1997).

[45]F. P. Incropera, D. P. DeWitt, T. L. Bergman, and A. S. Lavine, *Fundamentals of Heat and Mass Transfer*, Vol. 6 (Wiley New York, 2007).

[46]H.-R. Liu, K. L. Chong, Q. Wang, C. S. Ng, R. Verzicco, and D. Lohse, "Two-layer thermally driven turbulence: mechanisms for interface breakup," J. Fluid Mech. **913**, A9 (2021).

[47]J. Slattery, *Advanced Transport Phenomena* (Cambridge University Press, 1999).

[48]D. Juric and G. Tryggvason, "Computations of boiling flows," Int. J. Multiphas. Flow **24**, 387–410 (1998).

[49]S. Tanguy, T. Ménard, and A. Berlemont, "A level set method for vaporizing two-phase flows," J. Comput. Phys. **221**, 837–853 (2007).

[50]L. Ceresiat and M. V. Papalexandris, "Assessment of thermal boundary models for large eddy

simulations of natural convection," Flow Turbul. Combust. **114**, 117–144 (2025).

[51]F. Nicoud and F. Ducros, "Subgrid-scale stress modelling based on the square of the velocity gradient tensor," Flow Turbul. Combust. **62**, 183–200 (1999).

[52]T. M. Eidson, "Numerical simulation of the turbulent Rayleigh–Bénard problem using subgrid modelling," J. Fluid Mech. **158**, 245–268 (1985).

[53]B. Lessani and M. V. Papalexandris, "Time-accurate calculation of variable density flows with strong temperature gradients and combustion," J. Comput. Phys. **212**, 218–246 (2006).

[54]P. D. Antoniadis, *Modeling and numerical simulatin of transient flows in superposed porous and pure-fluid layers* (PhD Thesis, UCLouvain, 2015).

[55]S. Balay and et al., "PETSc Web page," (2025).

[56]M. Georgiou and M. V. Papalexandris, "Turbulent mixing in T-junctions: the role of the temperature as an active scalar," Int. J. Heat Mass Tran. **115**, 793–809 (2017).

[57]O. Shishkina, R. Stevens, S. Grossmann, and D. Lohse, "Boundary layer structure in turbulent thermal convection and its consequences for the required numerical resolution," New. J. Phys. **12**, 075022 (2010).

[58]G. Grötzbach, "Spatial resolution requirements for direct numerical simulation of the Rayleigh-Bénard convection," J. Comput. Phys. **49**, 241–264 (1983).

[59]R. Stevens, R. Verzicco, and D. Lohse, "Radial boundary layer structure and Nusselt number in Rayleigh-Bénard convection," J. Fluid Mech. **643**, 495–507 (2010).

[60]S.-H. Peng, K. Hanjalic, and L. Davidson, "Large-eddy simulation and deduced scaling analysis of Rayleigh–Bénard convection up to Ra= 10^9," J. Turbul. **7**, N66 (2006).

[61]F. Heslot, B. Castaing, and A. Libchaber, "Transitions to turbulence in helium gas," Phys. Rev. A **36**, 5870 (1987).

[62]J. Carlier and M. V. Papalexandris, "Multiple steady states in laminar Rayleigh-Bénard convection of air," Fluids **9**, 7 (2024).

[63]C. Sun, Y.-H. Cheung, and K.-Q. Xia, "Experimental studies of the viscous boundary layer properties in turbulent Rayleigh-Bénard convection," J. Fluid Mech. **605**, 79–113 (2008).

[64]Y. Cengel and A. Ghajar, *Heat and Mass Transfer* (McGraw-Hill, 2015).

[65]L. Soucasse, B. Podvin, P. Rivière, and A. Soufiani, "Proper orthogonal decomposition analysis and modelling of large-scale flow reorientations in a cubic Rayleigh–Bénard cell," J. Fluid Mech. **881**, 23–50 (2019).

[66]H. Tennekes and J. L. Lumley, "A First Course in Turbulence," MIT (1972).

[67]J. J. Niemela, L. Skrbek, K. R. Sreenivasan, and R. J. Donnelly, "Turbulent convection at very high Rayleigh numbers," Nature **404**, 837–840 (2000).

[68]X. He, D. P. M. van Gils, E. Bodenschatz, and G. Ahlers, "Logarithmic spatial variations and universal f-1 power spectra of temperature fluctuations in turbulent Rayleigh-Bénard convection," Phys. Rev. Lett. **112**, 174501 (2014).